

Nektar++: Development of the Compressible Flow Solver for Large Scale Aeroacoustic Applications

Daniel Lindblad^{a,*}, João Isler^a, Margarida Moragues Ginard^b, Spencer J. Sherwin^a, Chris D. Cantwell^a

^a*Imperial College London, London, SW7 2AZ, United Kingdom*

^b*Basque Center for Applied Mathematics, Bilbao, 48009, Spain*

Abstract

A recently developed computational framework for jet noise predictions is presented. The framework consists of two main components, focusing on source prediction and noise propagation. To compute the noise sources, the turbulent jet is simulated using the compressible flow solver implemented in the open-source spectral/hp element framework Nektar++, which solves the unfiltered Navier-Stokes equations on unstructured grids using the high-order discontinuous Galerkin method. This allows high-order accuracy to be achieved on unstructured grids, which in turn is important in order to accurately simulate industrially relevant geometries. For noise propagation, the Ffowcs Williams - Hawkings method is used to propagate the noise between the jet and the far-field. The paper provides a detailed description of the computational framework, including how the different components fit together and how to use them. To demonstrate the framework, two configurations of a single stream subsonic jet are considered. In the first configuration, the jet is

*

Corresponding author. *E-mail address:* d.lindblad@imperial.ac.uk

treated in isolation, whereas in the second configuration, it is installed under a wing. The aerodynamic results for these two jets show strong agreement with experimental data, while some discrepancies are observed in the acoustic results, which are discussed. In addition to this, we demonstrate close to linear scaling beyond 100,000 processors on the ARCHER2 supercomputer.

Keywords:

Jet Noise; Discontinuous Galerkin; Scaling; Large Eddy Simulation; Ffowcs Williams - Hawkings; Acoustics; Installation Noise.

1. Introduction

Many fluid flows of engineering interest generate noise, either directly, or indirectly through interactions with nearby solid surfaces. Examples of this include the flow around cooling fans in computers [1], the flow around A-pillars and rear view mirrors on cars and trucks [2], the flow over wind turbine blades [3], the flow around the undercarriages of high-speed trains [4], and the flows generated by different parts of an aircraft, including high-lift systems [5, 6], fan- and turbine blades [7, 8], landing gears [5, 6], and the propulsive jet [9, 10, 11]. This type of aerodynamically generated noise will often be perceived as unpleasant, and can in some cases even be harmful. Therefore, there is a widespread need to understand and minimize the underlying noise sources.

The study of aerodynamically generated noise, known as aeroacoustics, saw a great surge in the middle of the last century. In the beginning, the motivation for studying aerodynamically generated noise came mainly from the aircraft industry, where it was realized that jetliners equipped with the

17 newly invented turbojet engine would be too loud for widespread use. This
18 led to an era of intense research both in the UK and the US, known as the
19 first golden age of aeroacoustics [12]. An important result that came out of
20 this era is that jet noise scales with the eight power of the jet velocity [13, 14],
21 whereas the jet propulsive power only varies with the third power of the jet
22 velocity. Accordingly, it is possible to reduce the jet noise by lowering the jet
23 velocity and increasing the diameter of the jet. This led to the introduction
24 of high-bypass ratio turbofan engines, which today are in widespread use in
25 commercial aviation. For a comprehensive overview of the theory developed
26 during the first golden age of aeroacoustics, the interested reader is referred
27 to [15].

28 As computers became more and more powerful, numerical predictions
29 of aerodynamically generated noise started to become possible. An early
30 example of this is the propeller and rotorcraft prediction codes developed
31 at NASA Langley [16, 17]. These codes did not explicitly resolve the flow
32 field, but instead required input from correlations, simplified aerodynamic
33 calculations, or experiments in order to estimate the loading on the blades,
34 which in turn translates into noise sources in the Ffowcs Williams - Hawkins
35 equation [18]. Later, in 1992, Sir Michael James Lighthill foresaw a second
36 golden age of aeroacoustics, this time driven by direct computations of the
37 aerodynamically generated noise sources using CFD [12]. This led to a new
38 field of aeroacoustics, known as computational aeroacoustics (CAA). The
39 progress of this field over the past three decades has been summarized in
40 several review papers, see e.g. [19, 20]

41 In general, CAA shares a lot of similarities with CFD, including the

42 need for robust numerical methods and accurate turbulence models for high-
43 Reynolds number flows. However, as pointed out by e.g. Tam [21], some of
44 the challenges faced by CAA are often not encountered in CFD, including
45 the need to accurately resolve the acoustic waves (whose amplitude often are
46 orders of magnitude smaller than the amplitude of the hydrodynamic waves),
47 the need to propagate the acoustic waves over very large distances without
48 significant dissipation and dispersion errors, and the need to resolve unsteady
49 phenomena over a wide frequency range. In addition to this, reflections
50 of acoustic or hydrodynamic waves against an artificial boundary, e.g. an
51 inlet or an outlet to the computational domain, can quickly contaminate the
52 acoustic part of the solution, rendering the whole simulation useless [22].
53 Therefore, numerical methods that are tailored to the needs of CAA have
54 been actively developed over the past decades. These include, but are not
55 limited to, the dispersion relation preserving (DRP) finite difference schemes
56 by Tam and Webb [23], the compact finite difference schemes by Lele [24],
57 the prefactored compact finite difference schemes by Ashcroft and Zhang
58 [25], the Navier-Stokes characteristic boundary conditions by Poinso and
59 Lele [26], the radiation boundary conditions by Tam and Dong [27], Dong
60 [28], and the non-reflecting boundary conditions by Giles [29].

61 The spatial discretization schemes mentioned above were all developed for
62 structured grids, and some of them rely on wide finite-difference stencils. Al-
63 though highly successful, the limitation of these schemes to structured grids
64 makes it hard to adopt them for more complex configurations. Unstructured
65 finite-volume schemes, on the other hand, are typically limited to second-
66 order accuracy in space. This raises the need for high-order unstructured

67 schemes in order to tackle complex configurations of industrial interest with
68 optimal efficiency [20].

69 The development of high-order methods for unstructured grids has seen
70 great progress over the past decades. Interestingly, much of this development
71 has not been done with aeroacoustics in mind, but rather for the purpose
72 of performing accurate direct numerical simulations (DNS) and large eddy
73 simulations (LES) of turbulent flows. Among the many high-order schemes
74 that have been developed, we find the discontinuous Galerkin (DG) method
75 [30, 31], the flux reconstruction (FR) method [32], the spectral-difference
76 (SD) method [33, 34, 35, 36], and the continuous Galerkin (CG) method
77 [37].

78 In recent years, the aforementioned high-order methods have started to
79 be applied for CAA, see, e.g., [38, 39, 40, 41, 42]. However, given the large
80 number of possible applications for CAA mentioned earlier, the potential
81 benefits of these methods remain largely unexplored. Therefore, there is a
82 need to further develop and test these methods in the context of CAA.

83 The purpose of this paper is to document a recently developed com-
84 putational framework for jet noise predictions based on the high-order DG
85 method [40, 42]. This framework is based on a hybrid approach, in which
86 the turbulent jet is first simulated using the open-source spectral/hp element
87 framework Nektar++ [43, 44]. After this, the far-field noise is computed us-
88 ing the Antares library [45, 46, 47]. Antares solves Formulation 1A [48] of
89 the Ffowcs Williams and Hawkings [18] equation in the time-domain using a
90 source-time dominant algorithm.

91 The present paper focuses on describing the setup of the framework using

92 Nektar++ and Antares. In particular, in section 2, the pre-processing steps
93 (section 2.1), numerical method (section 2.2), and the post-processing steps
94 (section 2.3) are described in detail. In section 4, the framework is then
95 applied to an isolated and installed jet (section 4.1), followed by a demon-
96 stration of the scaling properties of the compressible flow solver in Nektar++
97 (section 4.2). Finally, in section 5, some conclusions are drawn.

98 **2. Methodology**

99 *2.1. Pre-Processing*

100 In this section we will present the pre-processing steps that we use to set
101 up the jet noise simulations. An overview of these steps, including how they
102 are linked together, is provided in Fig. 1.

103 *2.1.1. CAD Preparation*

104 Similar to many other computer aided engineering (CAE) problems, the
105 starting point for our simulations is a CAD description of the geometry that
106 we want to analyze. Typically, this geometry contains some surfaces that
107 are not relevant to the aeroacoustic analysis, such as small features that we
108 do not wish to resolve and/or surfaces that are not in direct contact with
109 the fluid. In addition to this, the outer boundaries of the computational
110 domain are often missing from the CAD. Therefore, the first step in the pre-
111 processing pipeline is to clean up the CAD and add additional surfaces that
112 define the missing boundaries. To this end, we use the open-source software
113 Gmsh [49], which provides access to the OpenCASCADE CAD kernel. The
114 Gmsh software is in turn controlled through its Python API, which makes it
115 very convenient to automate the CAD preparation steps.

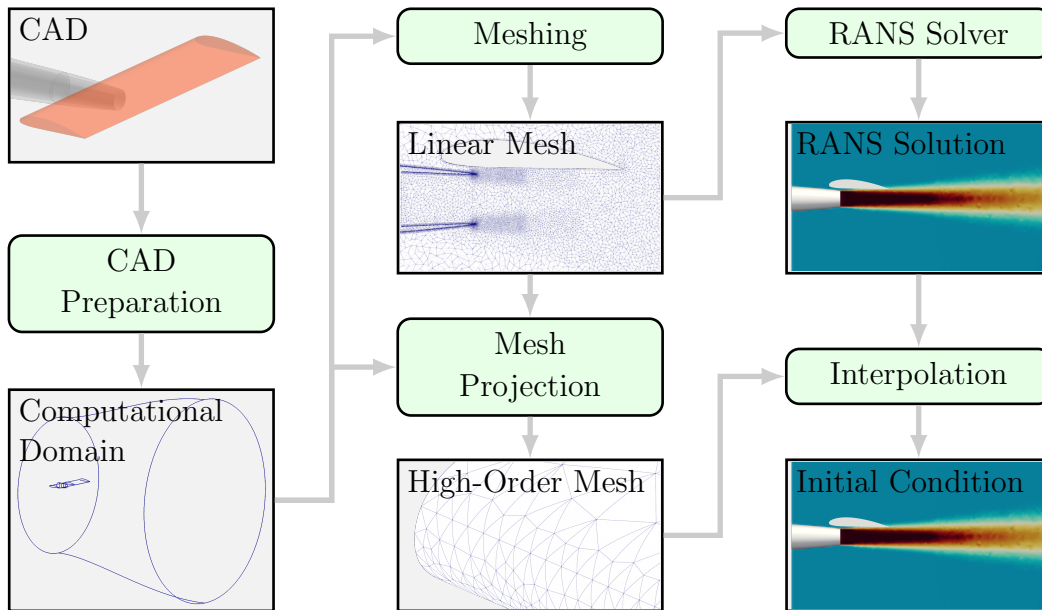


Figure 1: Flowchart illustrating the pre-processing setup.

116 *2.1.2. Mesh Generation*

117 The next step in the pre-processing pipeline is to generate a linear volume
 118 mesh. To this end, we use the commercial software STAR-CCM+ v2019.2. In
 119 particular, we use the *Advancing Layer Mesher* and the *Tetrahedral Mesher*
 120 in STAR-CCM+ to generate a single prism layer along solid walls, and tetra-
 121 hedral elements in the rest of the domain, respectively.

122 The use of an unstructured grid has two important advantages. Firstly,
 123 it can be used to mesh complex geometries with relative ease, which is im-
 124 portant in industrial applications. Secondly, it is straightforward to locally
 125 refine the mesh where it is needed, without having to refine other parts of the
 126 domain due to the constraints imposed by a structured grid. On the other

127 hand, when unstructured grids are used, it is very difficult to create high-
128 quality anisotropic mesh elements, which could be beneficial in some areas,
129 such as the early shear layer of the jet. However, recent work has found that
130 it is beneficial to use isotropic mesh elements in the early shear layer for jet
131 noise applications [50, 51]. Therefore, we believe that the current setup is
132 well suited for our purposes. If, however, we would like to switch to a hybrid
133 meshing strategy in the future, it is possible since Nektar++ also supports
134 hexahedral and pyramid elements.

135 After the linear volume mesh has been generated, the `NekMesh` utility
136 [44], which is part of the Nektar++ framework, is used to generate a high-
137 order mesh with several prism elements in the wall-normal direction. To this
138 end, the mesh is first projected onto the CAD by curving the mesh faces
139 that are in contact with the boundary such that they conform to the CAD
140 surface. After this, the curved prism elements are split in the wall-normal
141 direction using an isoparametric approach [52].

142 If the mesh elements attached to the boundary are highly anisotropic
143 and/or the underlying geometry is highly curved, it is possible that self-
144 intersecting elements are created during the CAD-projection step. To mini-
145 mize the risk of this happening, the aspect ratio of mesh elements adjacent
146 to a boundary must be carefully controlled during the meshing process. In
147 addition to this, the prism elements should be curved before they are split in
148 the wall-normal direction. For complex geometries, however, it is often hard
149 to completely eliminate the presence of invalid elements. To ensure that the
150 simulations can still be run, the `NekMesh` utility therefore provides a mod-
151 ule which can detect and remove the curvature from invalid elements. For

152 details on this, the interested reader is referred to the official documentation
153 [53].

154 The output of the mesh projection step is a high-order mesh that conforms
155 to the underlying CAD geometry. This mesh is written to an HDF5 file [54]
156 using the layout described in [44]. The HDF5 format is used since this
157 enables several processes to read parts of the mesh in parallel, which in turn
158 is necessary to efficiently partition the mesh in massively parallel simulations.

159 We finally note that the `NekMesh` utility can read mesh files in both the
160 `.ccm` format used by STAR-CCM+ and the `.msh` format used by Gmsh.
161 Therefore, any meshing software that supports one of these file formats can
162 be used in the pre-processing pipeline shown in Fig. 1.

163 *2.1.3. Initial Conditions*

164 In this work, we use the commercial software STAR-CCM+ v2019.2 to
165 compute the initial condition for the LES simulations. More precisely, STAR-
166 CCM+ is used to solve the Reynolds Averaged Navier Stokes (RANS) equa-
167 tions using the $k - \omega$ SST turbulence model. For the RANS simulations,
168 we use the same mesh topology as for the LES simulations. However, since
169 STAR-CCM+ uses a finite volume discretization, whereas Nektar++ uses
170 a high-order discontinuous Galerkin discretization, we typically use a finer
171 mesh for the RANS simulations.

172 In order to interpolate the RANS solution onto the high-order expansion
173 used in the LES simulations, the RANS solution is first interpolated
174 to the mesh vertices and written to a `.csv` file. After this, we use the
175 `FieldConvert` utility, which is part of the Nektar++ framework, to inter-
176 polate the point cloud defined by the `.csv` file onto the polynomial expansion

177 sion used in the LES simulations. More precisely, the field values are first
178 interpolated onto the quadrature points inside each element, followed by an
179 elemental projection in which the point values are converted to the corre-
180 sponding modal coefficients. Since the RANS solution is relatively smooth,
181 and because it only represents the initial conditions for the LES simulations,
182 we typically project it onto a linear polynomial basis ($p = 1$). More details
183 about how to use the interpolation routines in `FieldConvert` can be found
184 in the official documentation [53].

185 The interpolated solution is then written to a HDF5 file [54] using the
186 layout described in [44]. The HDF5 format is used to export the high-order
187 solution for the same reason that it is used to export the mesh, namely to
188 enable parallel I/O where each process only reads a subset of the solution
189 during initialization of the solver.

190 It is important to emphasize that there are other options for defining
191 initial conditions to the simulation. In particular, if another RANS solver
192 is available, it can easily be plugged into the pre-processing pipeline shown
193 in Fig. 1 as long as it can export the solution in the `.csv` format. In
194 addition to this, Nektar++ allows the user to define the initial conditions
195 using analytical expressions. Note that, in this case, there is no need to
196 write the initial conditions to file. Instead, the initial conditions can be
197 added directly to the input files for Nektar++. For more details on this, the
198 interested reader is referred to the official documentation [53].

199 *2.2. Numerical Method*

The flow is modeled by the compressible Navier-Stokes equations written in conservative form

$$\frac{\partial \mathbf{q}}{\partial t} + \frac{\partial}{\partial x_i} (\mathbf{f}_i^c(\mathbf{q}) - \mathbf{f}_i^v(\mathbf{q}, \nabla \mathbf{q})) = 0, \quad (1)$$

200 where $\mathbf{q} = (\rho, \rho u_1, \rho u_2, \rho u_3, E)^T$ is the vector of conservative variables, $\mathbf{f}_i^c(\mathbf{q})$
201 is the convective flux in the i^{th} direction and $\mathbf{f}_i^v(\mathbf{q}, \nabla \mathbf{q})$ is the diffusive flux
202 in the i^{th} direction. In this work, we assume that the gas is calorically perfect
203 and obeys the ideal law. In addition to this, we assume that the viscosity
204 is constant and equal to the far-field value outside the jet. This assumption
205 is valid since we only consider cold jets whose temperature is close to the
206 ambient temperature.

207 *2.2.1. Spatial Discretization*

208 The DG method is used to discretize Eq. (1) on a fully unstructured mesh
209 [55]. The diffusion terms are treated with the incomplete Interior Penalty
210 (IP) method [56] and the advection terms are rewritten using a standard weak
211 DG scheme, followed by the application of Roe's approximate Riemann solver
212 to compute the convective flux across the element boundaries [57, 58]. A
213 detailed explanation of how to define the spatial discretization in Nektar++
214 is provided in the official documentation [53].

215 In traditional LES, subgrid-scale models are used to model the coupling
216 between the resolved and the unresolved turbulent scales. However, by using
217 the Roe Riemann solver for coupling between adjacent elements, the solu-
218 tion is inherently diffused by the numerical discretization introduced by the
219 upwinding. This dissipation tends to smooth out high-frequency features

220 and suppress small-scale turbulent fluctuations. As a result, the unresolved
 221 turbulent scales are implicitly handled through the dissipation introduced by
 222 the discretization scheme. Previous work has shown that the DG discretiza-
 223 tion in combination with Roe’s approximate Riemann solver is well suited
 224 for implicit Large Eddy Simulations (iLES) [59, 60, 61, 62, 63, 64, 65].

In order to stabilize the solution in regions where the resolution is not high enough, an artificial viscosity approach is used. This stabilization strategy works by augmenting the dynamic viscosity and the thermal conductivity by an artificial viscosity and thermal conductivity in under-resolved regions. The artificial viscosity and thermal conductivity are respectively defined as

$$\mu_{av} = \mu_0 \rho \frac{h}{P} (c + \sqrt{u_k u_k}) S, \quad (2)$$

$$\kappa_{av} = \mu_{av} \frac{C_p}{Pr}, \quad (3)$$

225 where μ_0 controls the magnitude of μ_{av} , S is the sensor, C_p is the specific
 226 heat and Pr is the Prandtl number.

A sensor is used to make sure that the artificial viscosity and thermal conductivity are only activated in under-resolved regions. The sensor used in this work is a modal resolution based sensor [66]. To compute this sensor, the following resolution indicator is first computed.

$$s_e = \log_{10} \left(\frac{\langle u - \hat{u}, u - \hat{u} \rangle}{\langle u, u \rangle} \right), \quad (4)$$

where $\langle \cdot, \cdot \rangle$ is the L_2 inner product, u is the full expansion of a state variable (density in our case) of order P . Lastly, \hat{u} is the truncated expansion with terms up to $P - 1$. Based on the resolution indicator, the sensor is computed

as

$$S = \begin{cases} 0 & s_e < s_0 - \kappa, \\ \frac{1}{2} \left(1 + \sin \left(\frac{\pi(s_e - s_0)}{2\kappa} \right) \right) & |s_e - s_0| \leq \kappa, \\ 1 & s_e > s_0 + \kappa, \end{cases} \quad (5)$$

227 where $s_0 = s_k - 4.25 \log_{10}(P)$. Note that, the parameters s_κ and κ have to be
228 chosen in the correct range in order to make the artificial viscosity effective.

229 2.2.2. Temporal Discretization

230 The set of ordinary differential equations (ODEs) obtained from the spa-
231 tial discretization are integrated in time using a second-order singly diago-
232 nally implicit multi-stage Runge–Kutta (SDIRK2) method [67]. The nonlin-
233 ear system from SDIRK2 is iteratively solved by the Jacobian-free Newton
234 Krylov (JFNK) method [55]. Thus, the Newton method is used to solve the
235 nonlinear system [68]. The restarted generalized minimal residual method
236 (GMRES) [69] is adopted to solve the linear system. A Jacobian-free method
237 is applied in order to avoid explicitly calculating and storing the Jacobian
238 matrix [68].

239 In addition, a preconditioner in GMRES is employed which is important
240 for solving stiff problems. The parameters used to set up the preconditioner
241 are shown in listing 1, where `PreconMatFreezNumb` specifies number of
242 iteration that the GMRES solver will perform before the preconditioner ma-
243 trix be updated, `NonlinIterTolRelativeL2` is the convergence toler-
244 ance of the nonlinear system relative to the initial nonlinear system residual,
245 `LinSysRelativeTolInNonlin` represents the convergence tolerance of
246 the linear system solver in each nonlinear iteration. `PreconItsStep` de-

247 termines the number of preconditioning iterations to calculate the precondi-
248 tioned vector. For further understanding of the mathematical formulation of
249 these parameters, the reader may find useful the work of Yan et al. [55].

250 It is worth mentioning that the parameters shown in Listing 1 have a
251 strong impact on the convergence and efficiency of the implicit solver, and
252 consequently speed up the simulation. Special attention should be given
253 to the `PreconMatFreezNumb` parameter, since if its value is too low the
254 preconditioner matrix may be updated in every time-step, which reduces
255 the efficiency. However, large values may lead to divergence since the pre-
256 conditioner matrix is not updated as frequently as the numerical simulation
257 requires, making the preconditioner less effective at every time step. The
258 `PreconItsStep` parameter may significantly reduce the number of GM-
259 RES and nonlinear iterations when its value is increased; the time per time-
260 step increases but it allows for larger time steps which speeds up the simu-
261 lation overall. Therefore, the appropriate balance of these two parameters is
262 essential for the efficient execution of the numerical simulation.

```
263 <SOLVERINFO>  
264   <!-- This part is put inside the <CONDITIONS> tag -->  
265   <P> PreconMatFreezNumb      = 1000   </P>  
266   <P> NonlinIterTolRelativeL2 = 1.0E-3 </P>  
267   <P> LinSysRelativeTolInNonlin = 5.0E-2 </P>  
268   <P> PreconItsStep          = 3       </P>  
269 </SOLVERINFO>
```

Listing 1: Parameters for the preconditioner.

270 2.2.3. Boundary Conditions

271 Boundary conditions can have a large impact on the stability and accuracy
272 of a simulation. In LES simulations of jet noise, three types of boundaries

273 are typically present; solid walls, far-field boundaries, and inlet(s) to the
274 nozzle. In this section we will describe the implementation of these boundary
275 conditions in detail.

276 The far-field boundaries are used to impose the ambient conditions of the
277 flow, far away from the jet. The way the ambient conditions are imposed
278 depends on whether the flow enters or exits the domain through the boundary.
279 Along the parts of the far-field boundary where the flow enters the domain,
280 the far-field state is imposed using the *Weak-Riemann* approach described
281 in [57]. In this approach, the inviscid flux across boundary faces is computed
282 from the solution of a Riemann problem, using the far-field state and the
283 internal solution as the "left" and "right" state, respectively. This boundary
284 condition is non-reflective for normally incident waves as long as the Rie-
285 mann solver correctly differentiates between incoming and outgoing waves.
286 The Riemann solver used in this work approximately satisfies this condition.
287 Despite not being perfectly non-reflective, the amount of reflections against
288 this boundary is deemed to be negligible since the far-field boundary is placed
289 far away from the jet, and because the mesh is coarsened as it approaches
290 the far-field boundary.

291 At the outlet part of the far-field boundary, the *Weak-Riemann* approach
292 is also used. However, in contrast to the inlet part of the boundary, only the
293 ambient pressure is imposed. This is done by setting the left state in the
294 Riemann problem to be the internal solution, but with the pressure substi-
295 tuted for the ambient pressure [57]. This boundary condition is reflective.
296 Therefore, it is important that all waves are attenuated before they reach this
297 boundary. If only mesh coarsening is used for this purpose, an excessively

298 long computational domain would need to be used. To avoid this, we add a
 299 sponge zone upstream of the outlet [70]. In this zone, the right hand side of
 300 Eq. (1) is augmented with a damping term given by

$$\dots = -\sigma(\mathbf{x})(\mathbf{q} - \bar{\mathbf{q}}). \quad (6)$$

301 Here, $\sigma(\mathbf{x})$ is a function that controls the magnitude of the damping and $\bar{\mathbf{q}}$
 302 is a steady reference solution. In this work, the RANS solution that we use
 303 to initialize the simulations is also used to define $\bar{\mathbf{q}}$.

304 As explained in [22], the best results are obtained when the function
 305 $\sigma(\mathbf{x})$ is increased slowly over a sufficiently long distance. To achieve this, we
 306 compute it as

$$\sigma(\mathbf{x}) = \begin{cases} 0 & x_1 < x_{s_1}, \\ \sigma_{\max} S\left(\frac{x_1 - x_{s_1}}{x_{s_2} - x_{s_1}}\right) & x_1 \in (x_{s_1}, x_{s_2}), \\ \sigma_{\max} & x_1 > x_{s_2}. \end{cases} \quad (7)$$

307 Here, (x_{s_1}, x_{s_2}) denotes the interval where the sponge is increased (the jet
 308 is aligned with the x_1 -axis), σ_{\max} is the maximum value of the damping
 309 coefficient, and $S(\xi)$ is the smooth-step function

$$S(\xi) = 6\xi^5 - 15\xi^4 + 10\xi^3, \quad \xi \in (0, 1). \quad (8)$$

310 The smooth-step function is shown in Fig. 2. As can be seen from this figure,
 311 it increases smoothly from 0 to 1 over the interval $(0, 1)$.

312 The sponge zone is activated in Nektar++ by adding the commands
 313 shown in Listing 2 and Listing 3 under the <CONDITIONS> tag and the

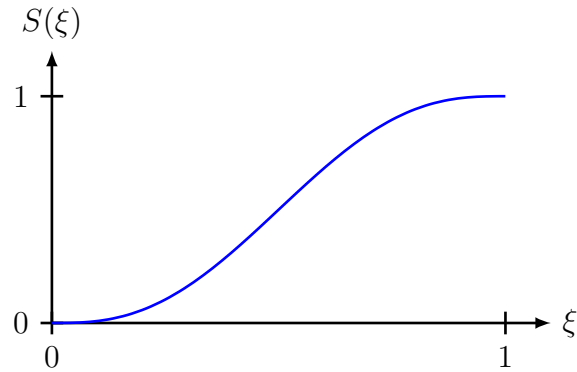


Figure 2: Smooth-step function.

314 <FORCING> tag in the input file, respectively. Note that these commands
 315 require that the parameters `x1`, `x2`, and `sigma_max` have been defined under
 316 the <PARAMETERS> tag in the input file.

```

317 <!-- This part is put inside the <CONDITIONS> tag -->
318 <FUNCTION NAME="AverageSolution">
319     <F VAR="rho,rhou,rhov,rhow,E" FILE="avg.fld" />
320 </FUNCTION>
321
322 <FUNCTION NAME="DampingCoeff">
323     <E VAR="rho,rhou,rhov,rhow,E" VALUE="-sigma_max*((x>x1)*(x<x2)*(6*((x-x1)/(x2
324     -x1))^5 - 15*((x-x1)/(x2-x1))^4 + 10*((x-x1)/(x2-x1))^3 + (x>=x2))" />
325 </FUNCTION>

```

Listing 2: Definition of average solution and damping coefficient.

```

326 <!-- This part is put inside the <FORCING> tag -->
327 <FORCE TYPE="Absorption">
328     <REFFLOW> AverageSolution </REFFLOW>
329     <COEFF> DampingCoeff </COEFF>
330 </FORCE>

```

Listing 3: Definition of sponge zone.

331 The length of the sponge zone is set to $20D_j$, where D_j is the diameter
 332 of the jet. The damping coefficient, which has a unit equal to s^{-1} , is then
 333 selected such that it is proportional to the reciprocal of the residence time of a
 334 convected disturbance inside the sponge zone. For the simulations presented
 335 in this work, we found that a value of

$$\sigma_{\max} = 10 \frac{U_j}{x_{s_2} - x_{s_1}}, \quad (9)$$

336 where U_j is the velocity of the jet at the nozzle exit, worked well.

337 At the inlet to the nozzle, we impose the stagnation pressure, stagnation
 338 temperature, and the flow direction. This boundary condition is chosen
 339 because in most experiments, including the ones used to validate the simula-
 340 tions performed in this work, the stagnation conditions are known upstream
 341 of the nozzle exit. The flow direction, on the other hand, is typically not
 342 known. Therefore, we set the flow direction equal to the boundary normal
 343 direction.

344 The inlet boundary condition is also imposed weakly through the Rie-
 345 mann solver. To this end, the 4 variables imposed by the boundary condition
 346 must be combined with one variable from the interior in order to form a com-
 347 plete left state for the Riemann solver. Depending on which interior variable
 348 is "extrapolated", the flow will develop in a different way from a given initial
 349 condition. For the simulations presented in this paper, it was found that
 350 extrapolating the magnitude of the velocity gave good stability. More pre-
 351 cisely, the left state in the Riemann solver is computed as follows. First, the
 352 temperature at the boundary is computed from the imposed stagnation tem-
 353 perature and the magnitude of the velocity taken from the interior, following

354 the definition of the stagnation temperature

$$T_{\text{BC}} = T_{0,\text{BC}} - \frac{1}{2C_p} u_{\text{R}}^2. \quad (10)$$

355 Here, $u_{\text{R}} = \sqrt{u^2 + v^2 + w^2}$ is the magnitude of the velocity obtained from the
 356 interior solution and C_p is the specific heat capacity. After this, the density
 357 is computed using the well known isentropic flow relation

$$\rho_{\text{BC}} = \rho_{0,\text{BC}} \left(\frac{T_{\text{BC}}}{T_{0,\text{BC}}} \right)^{\frac{1}{\gamma-1}}, \quad (11)$$

358 where R is the specific gas constant, γ the ratio of specific heats, and $\rho_{0,\text{BC}} =$
 359 $\frac{p_{0,\text{BC}}}{RT_{0,\text{BC}}}$ is the stagnation density. Finally, the left state at the boundary is
 360 defined as

$$\mathbf{q}_{\text{L}} = \begin{bmatrix} \rho_{\text{BC}} \\ \rho_{\text{BC}} u_{\text{R}} \mathbf{n} \\ \frac{p_{\text{BC}}}{\gamma-1} + \frac{1}{2} \rho_{\text{BC}} u_{\text{R}}^2 \end{bmatrix}. \quad (12)$$

361 Here, $\mathbf{n} = (n_1, n_2, n_3)$ is the imposed flow direction and $p_{\text{BC}} = \rho_{\text{BC}} R T_{\text{BC}}$ is
 362 the static pressure.

363 To use the inflow boundary condition described above, the commands
 364 shown in Listing 4 are added under the <BOUNDARYCONDITIONS> tag in
 365 the input file. In this listing, rho0 is the stagnation density, (n1, n2, n3)
 366 define the flow direction, and E0 = $p_{0,\text{BC}}/(\gamma - 1)$ is the stagnation total
 367 energy. These parameters must be defined inside the <PARAMETERS> tag
 368 in the input file.

```
369 <!-- This part is put inside the <BOUNDARYCONDITIONS> tag -->
370 <REGION REF="ID">
371   <D VAR="rho" USERDEFINEDTYPE="StagnationInflow" VALUE="rho0" />
```

```

372 <D VAR="rho" USERDEFINEDTYPE="StagnationInflow" VALUE="n1" />
373 <D VAR="rho" USERDEFINEDTYPE="StagnationInflow" VALUE="n2" />
374 <D VAR="rho" USERDEFINEDTYPE="StagnationInflow" VALUE="n3" />
375 <D VAR="E" USERDEFINEDTYPE="StagnationInflow" VALUE="E0" />
376 </REGION>

```

Listing 4: Definition of stagnation inflow boundary condition.

377 To save computational resources, we only include a short part of the nozzle
378 in our simulations. As a result, the boundary layer does not have enough
379 time to develop between the inlet and the end of the nozzle. To overcome
380 this issue, we impose non-uniform profiles of stagnation temperature and
381 pressure at the inlet. This can be done by passing a file containing the
382 boundary expansion of ρ_0 and E_0 to the boundary condition. Alternatively,
383 analytical expressions describing the spatial variation of ρ_0 and E_0 can be
384 used instead of the constant values shown in Listing 4.

385 To construct a file containing the boundary expansion of ρ_0 and E_0 ,
386 we start by extracting the mesh elements defining the boundary using the
387 `extract` module in NekMesh (see section 4 in the official documentation
388 for details [53]). After this, the resulting mesh file is edited to ensure that
389 the boundary expansion defined in the file uses the same polynomial order
390 as the one that will be used in the simulations. An example of this is for a
391 mesh containing quad and triangular elements is provided in Listing 5.

```

392 <!-- This part is put inside the <NEKTAR> tag -->
393 <EXPANSIONS>
394 <E COMPOSITE="C[0]" TYPE="MODIFIED" NUMMODES="2" FIELDS="rho,E" />
395 <E COMPOSITE="C[1]" TYPE="MODIFIED" NUMMODES="2" FIELDS="rho,E" />
396 </EXPANSIONS>

```

Listing 5: Expansion definition for an inlet containing quad and triangular elements.

397 After the expansion definition has been edited, the quadrature points are
398 exported to a `.csv` file using `FieldConvert`. By default, `FieldConvert`
399 will export data on a uniform set of points for visualization purposes. How-
400 ever, since we want to project data on the quadrature points back onto
401 the polynomial expansion, we need to export the location of the quadrature
402 points instead. To do this, the flag `--noequispaced` should be passed
403 to `FieldConvert`. After this, we use Python to compute the values of ρ_0
404 and E_0 at the location of the quadrature points. Note that, if an analytical
405 expression is used for this purpose, it is simpler to specify this expression
406 directly in the input file. In this work, however, we specify the profiles of
407 ρ_0 and E_0 using experimental data. More precisely, we use `SciPy` [71] to
408 interpolate the experimental data to the location of the quadrature points.
409 After this, we write the coordinates of the quadrature points together with
410 the associated values of ρ_0 and E_0 to a new `.csv` file. A new field file con-
411 taining the boundary expansions of ρ_0 and E_0 can then be obtained using
412 the `pointdatatofld` module in `FieldConvert`.

413 The implementation of the solid wall-boundary condition used for the
414 nozzle walls is described in detail in [57].

415 *2.3. Post-Processing*

416 In this section we describe the different tools that we use to post process
417 the solution. In particular, the technique used to propagate the noise between
418 the jet and the far-field observers is described in section 2.3.2. It does in turn
419 depend on the data collection strategy described in section 2.3.1.

420 *2.3.1. Data Collection*

421 Nektar++ provides a set of filters that can be used to compute derived
422 quantities from the solution. In this work, we make extensive use of the
423 history points filter to probe the solution at a set of predefined points. By
424 default, the history point filter writes the data to a `.csv` file every N^{th} time
425 step. If a small number of points is used, this is usually not a problem.
426 However, as more and more points are added, the I/O quickly starts to
427 consume a significant portion of the overall execution time. In addition to
428 this, the `.csv` format can not be used to store complex data structures, it
429 requires a relatively large amount of memory per data point, and it does not
430 allow the user to easily add additional metadata to the file. To overcome
431 these limitations, the history point filter in Nektar++ was extended to store
432 the points in the HDF5 format [54].

433 The HDF5 format is a flexible data format that allows the user to design
434 the layout of the file based on the needs of a particular application. To this
435 end, the HDF5 group provides the HDF5 library, which gives the user access
436 to a rich API that can be used to create, structure, and read/write large
437 amounts of data to the file.

438 The file structure chosen to store the history points is illustrated in Fig. 3.
439 The folders shown in this figure represent HDF5 groups. These groups are
440 synonymous to folders in a file system, in the sense that they can be used
441 to organize data inside the file. Starting from the root group, which we
442 call NEKTAR, two sub-groups are added. The first is called COORDINATES
443 which, as the name suggests, contains the coordinates of history points stored
444 as three HDF5 datasets. The second sub-group below the root group is called

445 TIME-DATA. Each time a new time step is written to the file, a new sub-
446 group called TIME-STEP-N is added to the TIME-DATA group, where N
447 is an integer which is incremented by one each time a new time step is
448 added. Inside this sub group, five HDF5 datasets are created, one per solution
449 variable. In addition to this, the current time is added as a HDF5 attribute.

450 The HDF5 format is well suited for post-processing since many popular
451 high-level programming languages, such as Python, Julia, and MATLAB, can
452 be used to read/write HDF5 files. Support for this functionality is usually
453 provided either directly, or through high-quality third-party packages. In
454 this work, we have used the h5py package to post-process the history point
455 data in Python. One example of this is provided in the next section.

456 2.3.2. *Far-Field Noise Predictions*

457 The overall goal of this work is to predict the far-field noise of turbulent
458 jets. Usually, the location where we want to measure the noise is located
459 outside the computational domain. Therefore, a separate method is needed
460 to propagate the noise between the jet and the far-field. In this work, we use
461 Antares 1.17.0 [45, 46, 47] for this purpose.

462 Antares solves the Ffowcs Williams - Hawkings equation [18] in the time
463 domain using a source-time dominant algorithm. The solution to the Ffowcs
464 Williams - Hawkings equation expresses the pressure signal at an arbitrary
465 observer location as an integral over a closed surface, plus a volume integral
466 over the volume outside the surface. In this work, we don't include the
467 volume integral in the solution to the Ffowcs Williams - Hawkings equation.
468 This simplification is widely used in jet noise applications [10, 11, 72], and
469 is valid as long as the integration surface is chosen such that it encloses

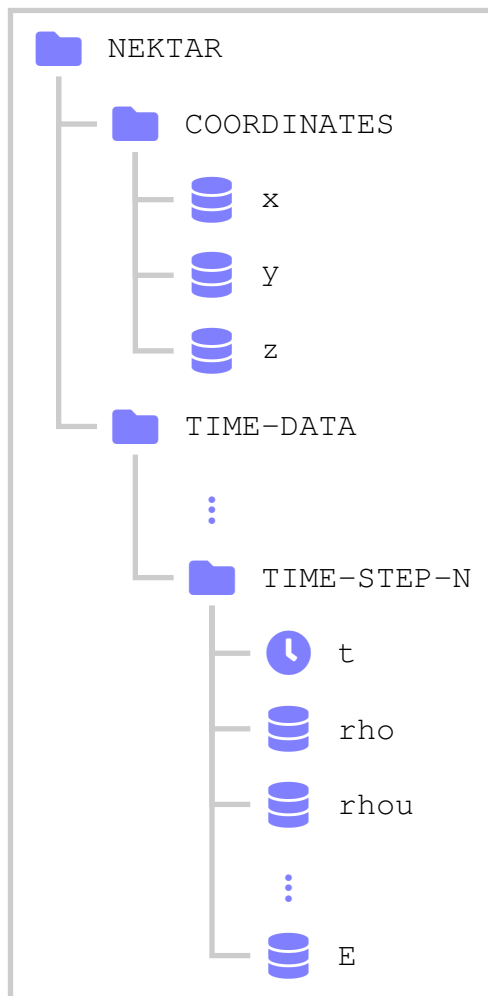


Figure 3: Layout of an HDF5 file storing history point data.

470 all relevant noise sources [73], and such that no entropy or vorticity waves
471 cross the surface [74, 75]. To satisfy these conditions, a conical surface that
472 follows the spreading rate of the jet is usually chosen [11]. Ideally, this
473 surface should be placed as close to the jet as possible in order to minimize
474 numerical dissipation and dispersion of the acoustic waves as they propagate
475 between the source and the surface. However, if the surface is too narrow,
476 the conditions stated above will be violated. Therefore, there is an optimal
477 width of the integration surface [10, 11].

478 In addition to adjusting the width, the length of the surface will influence
479 the accuracy of the results. Typically, a length of 30 nozzle diameters is
480 considered enough to enclose all relevant noise sources [72]. Unfortunately,
481 the entropy and vorticity waves generated in the jet do not decay over this
482 distance. Therefore, if the surface is closed at the downstream end, the sec-
483 ond condition stated above will be violated. As a result, spurious noise is
484 generated by the "end-cap" of the surface, which degrades the quality of the
485 results. One way to solve this problem is to extend the domain and the
486 integration surface much further, but since this also increases the compu-
487 tational cost, it is not desirable. Instead, alternative strategies such as the
488 method of end-caps [74], the pressure-formulation of the Ffowcs Williams
489 - Hawkings equation [74, 75], and the additional surface terms developed
490 by Rahier et al. [76], have been proposed. Unfortunately, the method of
491 end-caps and the additional surface terms proposed by Rahier et al. [76] are
492 not supported by Antares. In addition to this, the pressure formulation was
493 found to not improve the results for the cold jets considered in this work [40].
494 Therefore, a fourth strategy, in which the integration surface is left open at

495 the downstream end, is adopted instead. The benefit of this method is that
496 it eliminates spurious noise from the end-cap. However, this comes at the
497 cost of less accurate noise predictions for the lowest frequencies, see [74] for
498 details.

499 At present, Antares provides two solutions to the Ffowcs Williams -
500 Hawkings equation, Formulation 1A by Farassat [48] and Formulation 1C by
501 Najafi-Yazdi et al. [77]. The main difference between these two formulations
502 is that the latter includes the effect of a flight stream on noise propagation.
503 In this work, we only consider jets operating in a medium at rest. Therefore,
504 Formulation 1A is used.

505 To compute the noise propagation, we need the time history of the so-
506 lution on the integration surface. The process that we use to generate this
507 time history is illustrated in Fig. 4. It is important to point out that this
508 process is relatively generic, and will therefore work with any post-processing
509 software that implements the Ffowcs Williams - Hawkings method, as long
510 as this software can read one of the file formats that Nektar++ exports.

511 To begin with, the integration surface is constructed in Gmsh [49] using
512 the OpenCASCADE CAD kernel. After this, Gmsh is also used to create a
513 triangular surface mesh. The mesh resolution on the integration surface is
514 typically higher than the volume mesh. The reason for this is that Antares
515 does not support Gaussian quadrature on high-order elements. Instead, it
516 stores the data on the mesh vertices, and then compute the element con-
517 tribution as the average over all vertex values, scaled by the area of the
518 element.

519 To sample data on the integration surface, we use the history point filter

520 described in section 2.3.1. We start by converting the mesh generated with
521 Gmsh into the format used by Nektar++ using the NektMesh utility. By
522 default, NektMesh adds an XML tag to the mesh file that defines which
523 type of polynomial expansion, and which quadrature rule, to use for each
524 composite (group of mesh elements). Since Antares does not support high-
525 order elements, we edit the default expansion definition such that linear finite
526 elements are used. An example of this is provided in listing 6.

```
527 <!-- This part is put inside the <NEKTAR> tag -->  
528 <EXPANSIONS>  
529     <E COMPOSITE="C[0]" TYPE="MODIFIED" NUMMODES="2" FIELDS="u" />  
530 </EXPANSIONS>
```

Listing 6: Expansion definition for the Ffowcs Williams - Hawkings integration surface.

531 After the expansion definition has been edited, the quadrature points are
532 exported to a .csv file using the FieldConvert utility. As explained in
533 section 2.2.3, FieldConvert exports data on a uniform set of points instead
534 of the quadrature points by default. For a linear finite element expansion,
535 these points are simply the vertices of the elements. Although this is the data
536 that we eventually want to export to Antares, we do not want to sample the
537 solution at these points for reasons that will become clear soon. Therefore,
538 the flag `--noequispaced` is passed to FieldConvert when the points
539 are exported to the .csv file. The points defined in the .csv file are then
540 used by the history point filter to sample the solution at the integration
541 surface.

542 Once the simulation is finished, we need to convert the history point data
543 into a format that Antares can read. To this end, the Python script shown in
544 listing 7 is used. This script works by looping through all time steps stored

545 in the HDF5 file using the h5py package. For each time step, the script
 546 converts the solution to primitive variables, and stores the result in a tem-
 547 porary .csv file. The .csv file is then used by the process module called
 548 pointdatatofld, which projects data on the Gaussian quadrature points
 549 onto an existing expansion. Here, the existing expansion is stored in the
 550 field variable in the script, which in turn is obtained by reading the mesh
 551 file described earlier. Once the projection is completed, the updated expan-
 552 sion, which now contains 5 fields (one for each primitive variable) is written
 553 to a new file in the TecPlot binary format. Since the flag --noequispaced
 554 is not passed to FieldConvert this time, the solution will be exported on
 555 the mesh vertices instead of the quadrature points. Note that all these oper-
 556 ations are performed by directly calling the underlying Nektar++ functions
 557 through the NekPy module, which is provided together with Nektar++.

```

558 from NekPy.FieldUtils import Field, InputModule, ProcessModule, OutputModule
559 import h5py
560 import numpy as np
561
562 # Name of HDF5 file
563 hdf5_filename = "fwh-data.hdf5"
564
565 # Name of output file (in tecplot format)
566 plt_filename = os.path.splitext("fwh-data.plt")
567
568 # Name of mesh file (including expansion definition)
569 mesh_filename = "fwh-surface.xml"
570
571 # Open HDF5 file
572 with h5py.File(hdf5_filename, 'r') as hdf5_file:
573
574     # Read coordinates
575     cgroup = hdf5_file["NEKTAR/COORDINATES"]
576     x = cgroup["x"][:]

```

```

577 y = cgroup["y"][()]
578 z = cgroup["z"][()]
579
580 # Go through all time steps
581 tgroup = hdf5_file["NEKTAR/TIME-DATA"]
582 for indx, tstep in enumerate(tgroup.values()):
583
584     # Read solution at this time step
585     rho = tstep['rho'][()]
586     rhou = tstep['rhov'][()]
587     rhov = tstep['rhov'][()]
588     rhov = tstep['rhov'][()]
589     E = tstep['E'][()]
590
591     # Convert to primitive variables
592     u = rhou / rho
593     v = rhov / rho
594     w = rhov / rho
595     p = (E - 0.5 * (rhov**2 + rhov**2 + rhov**2)/rho) * 0.4
596
597     # Save data in .csv format
598     np.savetxt("tmp.csv", np.column_stack((x,y,z,rho,u,v,w,p)), delimiter=",",
599     , header="x, y, z, rho, u, v, w, p")
600
601     # Create a Nektar++ Field and read expansion from file
602     field = Field([])
603     InputModule.Create("xml", field, mesh_filename).Run()
604
605     # Project points to expansion
606     ProcessModule.Create("pointdatatofld", field, frompts="tmp.csv").Run()
607
608     # Save data to .plt format
609     output_filename = plt_filename[0] + "-%05i"%(index) + plt_filename[1]
610     OutputModule.Create("plt", field, output_filename).Run()

```

Listing 7: Python script for converting history point data into TecPlot binary format.

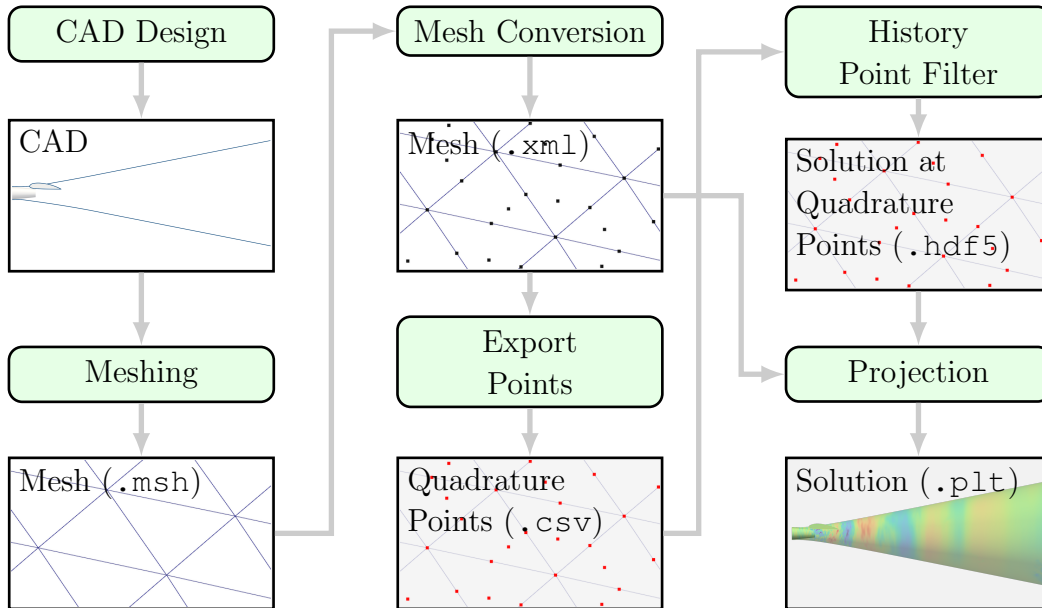


Figure 4: Flowchart illustrating the steps required to sample data on the integration surface used for the Ffowcs Williams - Hawkings method.

611 3. Performance considerations

612 *Parallelization.* Parallelization in Nektar++ is carried out using a domain
 613 decomposition strategy, where the computational mesh is divided into one
 614 subset per process. Mesh partitioning is achieved using either the Scotch
 615 or the METIS libraries at the beginning of the simulation. Note that each
 616 processor only reads the geometric information that is required for its own
 617 partition, that is, the partitioning of the mesh file is done in parallel. Par-
 618 allel mesh partitioning, contrary to serial mesh partitioning, avoids one sin-
 619 gular thread reading the whole mesh and partitioning it alone which could
 620 lead to the node running out of memory. This is achieved through the

621 use of HDF5 routines when reading the mesh datasets and the use of the
622 `--use-hdf5-node-comm` flag with Nektar++. Output solution files can
623 also be written in HDF5 format which is enabled by the flag `--io-format`
624 `Hdf5`. The different processes communicate through the standard MPI pro-
625 tocol, where each process is independently executed and there is no explicit
626 use of shared memory protocols such as OpenMP. In this work we use the
627 Scotch library to partition the mesh.

628 *Vectorization.* The limitation in performance of modern hardware concerns
629 memory bandwidth speeds more than processor clock speeds. For this reason,
630 the use of arithmetically intense schemes, that is, schemes performing a high
631 number of floating point operations for each byte transferred from memory,
632 continues to be of considerable interest. At high polynomial orders, high-
633 order or spectral/hp element methods are arithmetically intense schemes
634 since they involve dense, compact kernels for key finite element operators.
635 This is a significant advantage of high-order methods compared to lower-order
636 methods. Key aspects to exploit this potential for increased performance
637 are matrix-free implementations of finite element operators combined with
638 the use of sum-factorization and effective approaches for exploiting single-
639 instruction multiple-data (SIMD) vectorization. Nektar++ is provided with
640 the matrix-free evaluation of basic finite element operations which still utilize
641 sum-factorization even for non-tensor-product elements (triangles, tetrahe-
642 dra, and prisms) [78, 79, 80]. Nektar++ also allows explicit exploitation
643 of SIMD vectorization, showing that although performance is naturally de-
644 graded when going from hexahedra to triangles, tetrahedra, and prismatic
645 elements, efficient implementations are still obtained, achieving 50% to 70%

646 of the peak floating-point throughput of modern processors with both AVX2
647 and AVX512 instruction sets [81]. In addition to that, the SIMD vectoriza-
648 tion of the diffusion operator and the block diagonal matrix obtained after
649 decoupling the jacobian matrix to calculate the preconditioned vector has
650 recently been implemented in Nektar++. Also, the $(\hat{\mathbf{L}} + \hat{\mathbf{U}})$ matrix, which
651 is also obtained from the jacobian matrix, employed to calculate the precon-
652 ditioned vector is now able to use the auto-tuning routines (e.g. matrix free
653 operator) to optimize this operator. For further details about the precon-
654 ditioner calculation the reader is referring to [55]

655 *Automatic selection of the operations optimization.* An auto-tuning capa-
656 bility, to automatically select the most efficient operations optimization for
657 each execution, is also available in Nektar++ [80]. It can be turned on by
658 including the lines, given in Listing 8, in the problem setting script.

```
659 <NEKTAR>  
660   <!-- This is how to enable auto tuning -->  
661   <COLLECTIONS DEFAULT="auto"/>  
662 </NEKTAR>
```

Listing 8: Flag for enabling performance auto-tuning in Nektar++.

663 For more details on this, the interested reader is referred to the official doc-
664 umentation [53].

665 4. Results

666 4.1. Isolated and Installed Jet Noise

667 In this section we will present the application of the computational frame-
668 work presented in this paper to investigating noise generated by isolated and
669 installed jets.

670 *4.1.1. Case Description*

671 The nozzle considered in this work has an inner diameter of $D_j = 40\text{mm}$,
 672 a convergence half-angle of 2.44° , and a total length of $19D_j$. Both an isolated
 673 and an installed configuration are considered. In the installed configuration,
 674 an uniform-chord (2D) NACA4415 airfoil at 4° angle of attack is placed close
 675 to the nozzle. The axial and vertical distance between the nozzle exit and
 676 the airfoil trailing edge are $L = 3D_j$ and $H = 0.6D_j$, respectively. The chord
 677 and span of the airfoil are $3.75D_j$ and $15D_j$, respectively. A schematic view
 678 of the installed configuration is shown in Fig. 5.

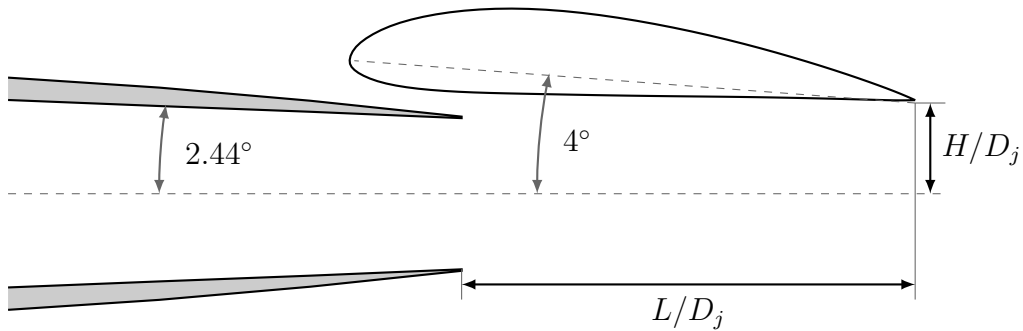


Figure 5: Schematic view of the nozzle installed under the wing.

679 In this work, we consider a single operating point of the nozzle, corre-
 680 sponding to an acoustic Mach number of $M_a = U_j/c_\infty = 0.6$, a Reynolds
 681 number of $Re_j = \rho_\infty U_j D_j / \mu_\infty = 5.5 \cdot 10^5$, and a static temperature ratio of
 682 $T_j/T_\infty = 0.9335$. In addition to this, no flight stream is considered, meaning
 683 that the ambient medium is at rest.

684 Both the isolated and installed configuration of the nozzle have recently
 685 been tested in the Doak Laboratory Flight Jet Rig, located at the University

686 of Southampton. During these tests, both aerodynamic data (velocity mea-
687 surements in the jet plume) and far-field acoustic data was recorded. This
688 data will be used in sections 4.1.3 and 4.1.4 to validate the simulations. More
689 details about the experimental setup can be found in [40, 42, 82].

690 4.1.2. Computational Setup

691 A schematic view of the axi-symmetric, funnel-shaped computational do-
692 main used in this work is presented in Fig. 6. Along the left and top boundary
693 shown in this figure, the far-field state is imposed using the *Weak-Riemann*
694 approach described in section 2.2.3. As indicated by the arrows in the
695 figure, a small co-flow corresponding to 2% of the jet exit velocity is also
696 added to the (stagnant) far-field state. This is done to ensure that vortical
697 structures generated in the jet are flushed out of the domain and to facilitate
698 flow entrainment.

699 Along the right boundary in Fig. 6, the ambient pressure is imposed
700 according to the method described in section 2.2.3. Since this boundary con-
701 dition is reflective, a sponge zone of length $20D_j$ is also added upstream of the
702 outlet boundary. In this region, the damping term described in section 2.2.3
703 is used to attenuate the jet before it reaches the outflow boundary.

704 The inlet to the nozzle is placed $1.5D_j$ upstream of the nozzle exit. At
705 this boundary, non-uniform profiles of stagnation pressure and temperature
706 are imposed to ensure that the mean velocity matches the experimental data
707 as closely as possible at the nozzle exit, see section 2.2.3 for details about
708 the implementation.

709 In addition to matching the mean velocity profile at the nozzle exit, re-
710 cent work has demonstrated the importance of getting the turbulence levels

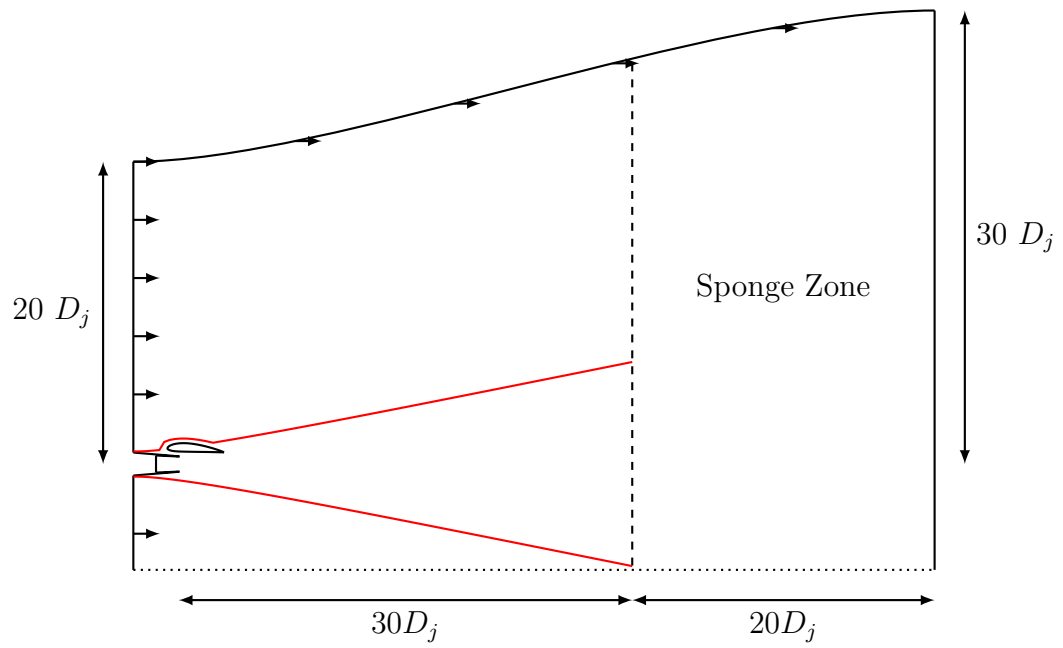


Figure 6: Schematic view of the computational domain and the Ffowcs Williams - Hawkings integration surface.

711 in the boundary layer right [50, 51, 83, 84]. In order to satisfy this condi-
712 tion, some type of artificial tripping mechanism and/or injection of synthetic
713 turbulence at the inlet boundary may be necessary when only a short part
714 of the nozzle is included in the simulations. In addition to this, for high
715 Reynolds number applications, it is usually necessary to model the inner
716 part of the boundary layer, either through the use of a wall model [50] or a
717 hybrid RANS-LES model [51, 85]. Unfortunately, Nektar++ currently does
718 not support any tripping mechanism, synthetic turbulence injection, or wall
719 model. Therefore, a standard no-slip boundary condition is used to model
720 the nozzle instead. In earlier work, we noted that the turbulence levels at
721 the nozzle exit are not accurately predicted with this setup [40, 42]. It is
722 well known that the state of the boundary at the nozzle exit can have a large
723 influence on the far-field acoustic results [50, 83, 84]. Therefore, a better wall
724 modeling strategy is expected to improve the results, but was unfortunately
725 outside the scope of this work.

726 The methodology described in section 2.1.2 was used to generate the two
727 unstructured meshes shown in Fig 7. As can be seen from this figure, the
728 main difference between these two meshes is that the latter includes the wing.
729 In addition to this, the resolution far downstream is slightly lower for the
730 second mesh. The resulting mesh count for the two meshes are summarized
731 in Table 1. More details about the two meshes are provided in [42].

732 Three simulations have been performed, one for the isolated jet, and
733 two for the installed jet. The simulation of the isolated jet was performed
734 with Mesh-1 using a polynomial degree of $P = 2$. The two simulations of
735 the installed jet were performed with Mesh-2, using a polynomial degree of

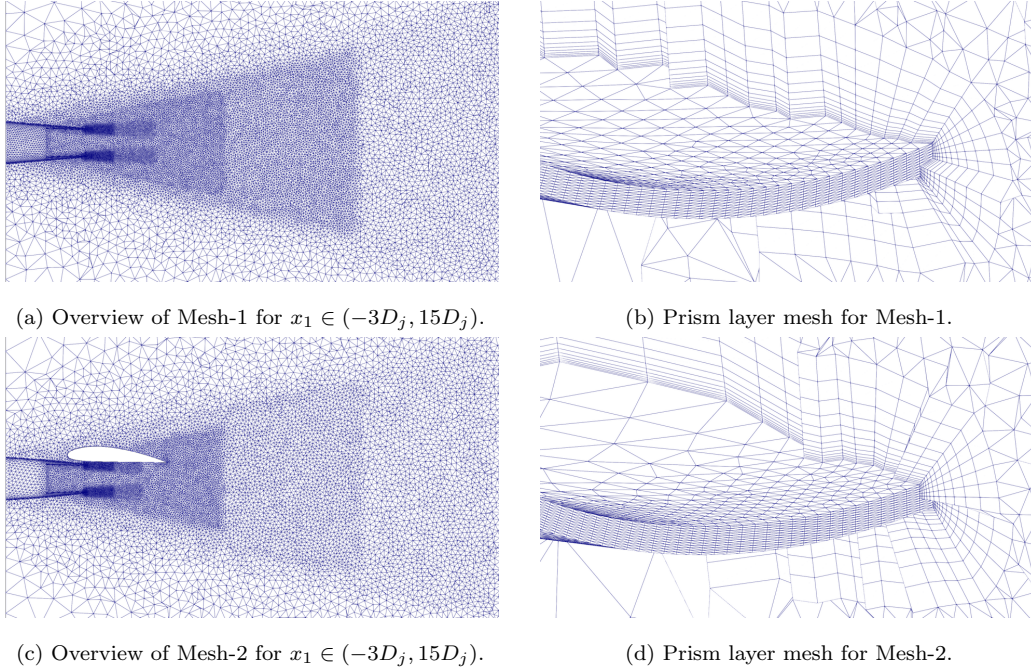


Figure 7: Illustration of unstructured grids defined in Table 1.

Table 1: Mesh settings.

Name	Configuration	N_{prism}	N_{tet}
Mesh-1	Isolated	$4.36 \cdot 10^5$	$6.18 \cdot 10^6$
Mesh-2	Installed	$4.63 \cdot 10^5$	$4.54 \cdot 10^6$

Table 2: Simulation settings. Δt_{jet} and $\Delta t_{\text{FW-H}}$ denote the sampling rate in the jet plume and on the Ffowcs Williams - Hawkins integration surface, respectively. τ_{init} and τ_{sample} denote the time the simulation is run before sampling and during sampling, respectively.

Name	P	Mesh	DOF	Initialize from	$\frac{\Delta t c_{\infty}}{D_j}$	$\frac{\Delta t_{\text{jet}} c_{\infty}}{D_j}$	$\frac{\Delta t_{\text{FW-H}} c_{\infty}}{D_j}$	$\frac{\tau_{\text{init}} c_{\infty}}{D_j}$	$\frac{\tau_{\text{sample}} c_{\infty}}{D_j}$
Isolated-1	2	Mesh-1	$70 \cdot 10^6$	RANS	0.002	0.04	0.04	350	320
Installed-1	2	Mesh-2	$54 \cdot 10^6$	RANS	0.002	0.04	0.04	450	900
Installed-2	3	Mesh-2	$109 \cdot 10^6$	Installed-1	0.002	0.04	0.04	300	450

736 $P = 2$ and $P = 3$, respectively. A summary of the settings used for each
737 simulation is presented in Table 2.

738 4.1.3. Aerodynamic Results

739 We start by considering the mean and RMS of the axial velocity in the
740 jet plume. The simulation results obtained for the isolated jet are compared
741 against experimental data in Figs. 8a and 8b. As can be seen from these
742 figures, the agreement is quite satisfactory for all radial and axial locations.
743 The most notable discrepancies are found close to the jet centerline and fur-
744 ther downstream. In this region, the mean velocity and turbulence levels are
745 over-predicted and under-predicted by the simulation, respectively. From
746 earlier work, we know that the state of the boundary layer at the nozzle exit
747 is not perfectly predicted in our simulations due to insufficient resolution and
748 lack of a wall-model [42]. Since the state of the boundary layer affects the
749 development of the shear layer, it is possible that the under-resolved bound-
750 ary layer contributes to the discrepancies seen far downstream in Figs.. 8a
751 and 8b. Another possible source of the discrepancies is that we only include
752 a short part of the conical nozzle in the simulations, which in turn should

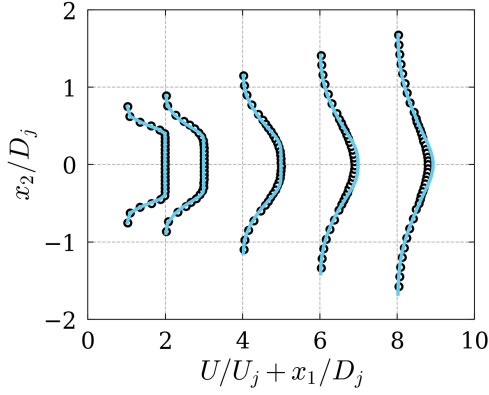
753 lead to slight discrepancies in the radial velocity component at the nozzle
754 exit. This is explained in more detail in [42].

755 The simulation results obtained for the installed nozzle are compared
756 against the corresponding experimental data in Fig. 8. In general, we can
757 note that the agreement between simulations and experiments is quite good
758 for the installed nozzle as well. It is also interesting to note that the higher
759 polynomial degree used in the simulation called "Installed-2" only has a mi-
760 nor impact on the flow statistics. Finally, we note that the discrepancies be-
761 tween the simulations and the experiments is consistent with those observed
762 for the isolated nozzle. This is expected, considering that the simulation
763 setup is almost identical for the two configurations.

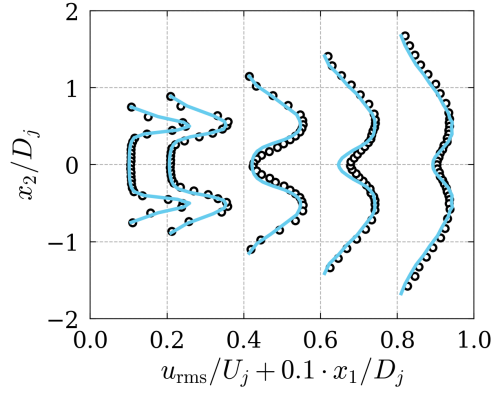
764 4.1.4. *Far-Field Acoustic Results*

765 As explained in section 2.3.2, we use the Ffowcs Williams - Hawkings
766 method implemented in Antares 1.17.0. to compute the far-field noise. The
767 output of Antares is the pressure signal at the same microphone locations as
768 were used in the experiments. The time-series signal is then converted into
769 a power spectral density (PSD) in units [dB/St] using the implementation of
770 Welch's method [86] in SciPy [71]. More details on the exact locations of the
771 microphones and how the PSD is computed can be found in [40, 42].

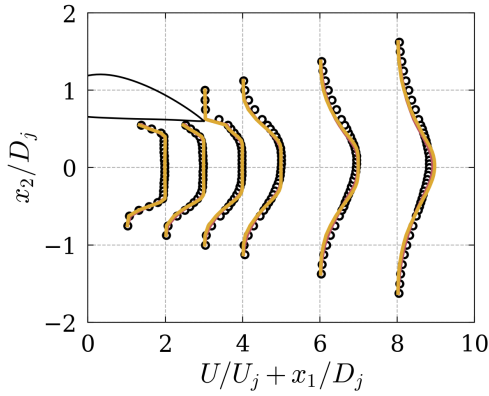
772 The PSD at two representative microphone locations located at $\theta = 90^\circ$
773 and 43° with regards to the downstream jet axis is presented in Fig. 9a and
774 9b, respectively. By comparing the results in these two figures, it is clear that
775 the simulations agree better with the experiments for the $\theta = 43^\circ$ angle. This
776 is expected since jet noise peaks at shallower angles [87]. From Fig. 9b, we
777 can also see that the effect of the wing is very small at $\theta = 43^\circ$. In contrast,



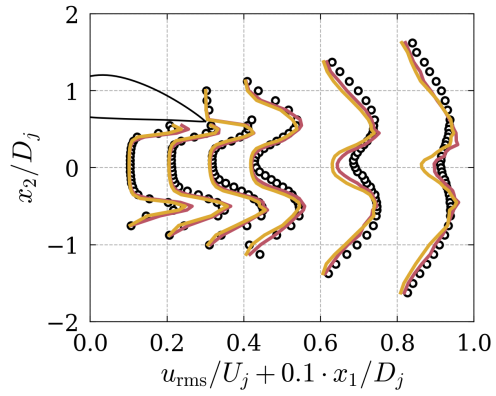
(a) Mean axial velocity for the isolated jet.



(b) RMS of axial velocity for the isolated jet.



(c) Mean axial velocity for the installed jet.



(d) RMS of axial velocity for the installed jet.

Figure 8: Velocity statistics in jet plume for the isolated and the installed jet. Isolated-1 (—), Installed-1 (—), Installed-2 (—), Experiments (○).

778 the far-field noise levels are considerably higher for the installed nozzle at the
779 $\theta = 90^\circ$ angle, especially for $St < 2$ (Fig. 9a). These results are explained by
780 the fact that jet installation noise has a dipole directivity that peaks in the
781 $\theta = 90^\circ$ and 270° direction [88].

782 Figures 9a and 9b show that the simulation of the isolated nozzle tends to
783 over-predict the corresponding experimental results, especially for the higher
784 frequencies. We believe these discrepancies can be partly explained by the
785 under-resolved boundary layer inside the nozzle. The resolution (mesh and
786 polynomial degree) might also be too low for the isolated nozzle. In fact, if
787 we compare the spectra obtained with the $P = 2$ and $P = 3$ simulation of
788 the installed nozzle, we see that the simulation with the higher polynomial
789 degree (Installed-2) gives lower noise levels for higher frequencies. Since jet
790 installation noise mostly contributes to the lower frequencies, it is likely that
791 the noise levels for the isolated jet would come down further if $P = 3$ was
792 used. Unfortunately, this turned out to be outside the scope of this paper.

793 Despite the improvement seen when going from $P = 2$ to $P = 3$ for
794 the installed nozzle, there are still some notable discrepancies in the far-
795 field spectra for the highest and lowest frequencies. The discrepancies seen
796 for the highest frequencies are likely caused by the same error sources as
797 for the isolated nozzle, e.g., insufficient modeling of the boundary layer and
798 resolution in the jet plume. Also, since the microphones are located below
799 the wing, the errors at the highest frequencies are amplified due to reflections
800 against the pressure side of the wing. With regards to the lowest frequencies,
801 on the other hand, the effect of the resolution along the wing span and size
802 of the Ffowcs Williams - Hawkings integration surface could be potential

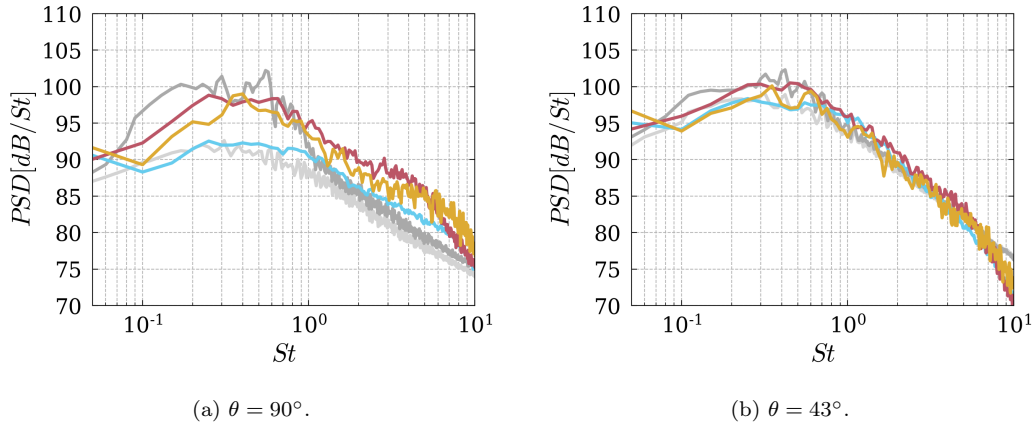


Figure 9: Power Spectral Density in the far-field. Isolated-1 (—), Installed-1 (—), Installed-2 (—), Experiments for isolated jet (—), Experiments for installed jet (—).

803 sources of error. The effect of these should be investigated in future work.

804 4.2. Scaling and performance

805 The scalability of Nektar++ has been demonstrated on a number of par-
 806 allel computers. In this case, strong scaling results of the compressible flow
 807 solver in Nektar++ on ARCHER2 and JUWELS supercomputers are pre-
 808 sented. The scaling plots are generated based on the time-integration com-
 809 putational time (whole application except initialization and I/O). This ap-
 810 proach is taken since the majority of time is spent on time-integration in a
 811 production run.

812 The DG method and 2nd order implicit time integration scheme intro-
 813 duced in sections 2.2.1 and 2.2.2, respectively, are considered for the scaling.
 814 The installed round nozzle case presented in sections 4.1.1 to 4.1.3 is used.
 815 This test has been run for 100 time steps on a mesh of approximately 5 mil-

816 lion elements. Two polynomial orders, $P = 2$ and $P = 3$, have been tested.
817 In total, this case contains approximately 54 million DOF for $P = 2$ and 109
818 million DOF for $P = 3$.

819 The scaling tests on ARCHER2 and JUWELS are presented in Fig. 10.
820 Tables including the timings of interest on ARCHER2 and JUWELS are
821 also presented in Table 3 and Table 4, respectively. It can be seen from
822 these figures that the scalings are done between 2,560 and 140,800 cores on
823 ARCHER2 and between 2,400 and 28,800 cores on JUWELS. ARCHER2 has
824 128 cores (2x AMD Zen2 Rome EPYC 7742 CPUs and 64 cores per CPU)
825 and 256 GB per node, while JUWELS has 48 cores (2x Intel Xeon Platinum
826 8168 Skylake CPUs and 24 cores per CPU) and 96 GB per node. We be-
827 lieve that the higher memory per node on ARCHER2 allowed us to use a
828 higher number of nodes compared to JUWELS. In Fig. 10 we observe a pro-
829 nounced super-linear scaling on ARCHER2 probably due to a larger number
830 of cache misses for small job sizes. This probably means that Nektar++
831 is not cache optimized [89]. We can conclude from the scaling results that
832 the optimal number of DOF per core is between 650 and 850. Below that,
833 parallel efficiency decreases.

834 5. Conclusions

835 In this paper, we have presented a computational framework for accu-
836 rately predicting jet noise. Our framework utilizes the spectral hp approach
837 of Nektar++ to simulate turbulent jets. To compute the noise propaga-
838 tion from the jet vicinity to the far-field, we employed the Ffowcs Williams -
839 Hawkings method, which is implemented in the Antares library. The primary

Table 3: Time-integration CPU time of the scaling runs done on ARCHER2.

Num. nodes	Num. cores	CPU time P=2	CPU time P=3
20	2560	1309.62	3083.04
50	6400	410.658	1066.50
100	12800	191.250	496.383
150	19200	123.885	308.756
200	25600	91.6463	221.697
250	32000	78.5870	176.408
300	38400	60.2471	140.109
350	44800	52.2270	120.575
400	51200	44.9938	105.134
450	57600	40.8790	95.1388
500	64000	37.6927	84.2975
550	70400	32.3210	-
600	76800	31.6789	70.1267
650	83200	29.4066	-
700	89600	30.5700	61.5184
800	102400	31.6817	52.5133
850	108800	-	49.4919
900	115200	-	47.9693
1000	128000	-	43.7558
1100	140800	-	53.4228

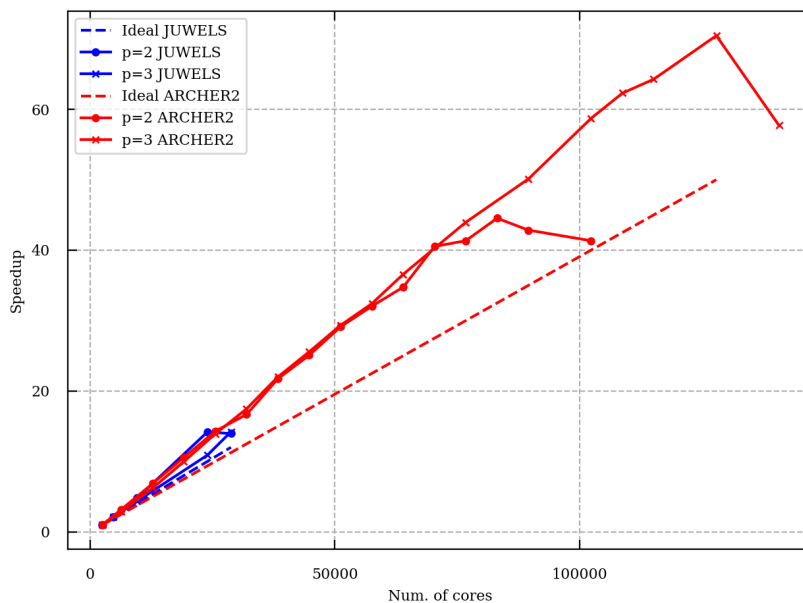


Figure 10: Strong scaling for the installed round nozzle case on ARCHER2, between 2,560 and 140,800 cores, and on JUWELS, between 2,400 and 28,800 cores, for polynomial orders $P = 2$ and $P = 3$.

840 objective of our work is to provide a comprehensive description of the com-
 841 putational framework developed, highlighting the integration of Nektar++
 842 with Antares to enable turbulent jet simulations and reliable predictions of
 843 jet noise.

844 To enable high-order simulations for turbulent jets and noise predictions,
 845 several important methodological aspects were discussed. Firstly, the gener-
 846 ation of high-order meshes that accurately conform to the underlying CAD
 847 geometry was described. Additionally, the importance of establishing com-
 848 patible initial and boundary conditions for high-order simulations was high-
 849 lighted. In terms of post-processing, we presented a data acquisition strategy
 850 focused on probing the solution. As part of this strategy, we extended the

Table 4: Time-integration CPU time of the scaling runs done on JUWELS.

Num. nodes	Num. cores	CPU time P=2	CPU time P=3
50	2400	919.817	1811.14
100	4800	435.883	870.604
200	9600	192.249	416.621
500	24000	64.8598	166.230
600	28800	65.9233	127.540

851 history point filter in Nektar++ to store points in HDF5 format. Finally, we
 852 addressed the process of generating the time history required for computing
 853 noise propagation using Antares.

854 To showcase the computational framework, two configurations of a single
 855 stream subsonic jet were computed. The first configuration focuses on an
 856 isolated jet nozzle, while the second configuration incorporates a NACA4415
 857 airfoil positioned near the nozzle exit. The numerical simulations were com-
 858 pared with experimental data provided by the University of Southampton.
 859 The numerical aerodynamic results demonstrated very good agreement with
 860 the experimental data. Small discrepancies were observed in the centreline
 861 of the jet and further downstream. These discrepancies may be explained
 862 by the under-resolved boundary layer and the inclusion of only a short part
 863 of the conical nozzle. In terms of far-field results, some discrepancies were
 864 observed between the simulations and the experiments. In particular, the
 865 simulations tend to over-predict the corresponding experimental results for
 866 the isolated nozzle, mainly for the highest frequencies. For the installed noz-
 867 zle, discrepancies in the far-field spectra were observed for the highest and

868 lowest frequencies. For the highest frequencies, the discrepancies were at-
869 tributed to the insufficient modeling of the boundary layer and resolution in
870 the jet plume in both cases. On the other hand, the discrepancies in the
871 lowest frequencies for the installed nozzle could potentially be caused by a
872 relatively low resolution along the wing span and size of the Ffowcs Williams
873 - Hawkings integration surface around the wing. These source errors will be
874 investigated in future work.

875 Recent developments in computational performance have resulted in sig-
876 nificant speed up for highly computationally intensive simulations. One note-
877 worthy development is the use of SIMD vectorization to calculate the diffu-
878 sion operator and preconditioner within the compressible implicit solver in
879 Nektar++. Furthermore, the scalability of the Nektar++ framework has
880 been demonstrated on ARCHER2 and JUWELS supercomputers. The scal-
881 ing results indicate linear scaling up to more than 100,000 cores for the
882 ARCHER2 supercomputer.

883 **Acknowledgements**

This work was supported by the European Union’s H2020 program under the DJINN (Decrease Jet INstallation Noise) project, Grant Agreement No. 861438, and the Marie Skłodowska-Curie individual fellowship, Grant Agreement No. 842536. Computational resources have been provided by the Partnership for Advanced Computing in Europe (PRACE) on the JUWELS cluster. This work also used the ARCHER2 UK National Supercomputing Service (<https://www.archer2.ac.uk>). The authors would like to acknowledge the Antares development team at CERFACS for providing the Antares library.



885 **References**

- 886 [1] L. Huang, Characterizing computer cooling fan noise, *The Journal of*
887 *the Acoustical Society of America* 114 (2003) 3189–3200. doi:10.1121/
888 1.1624074.
- 889 [2] N. Oettle, D. Sims-Williams, *Automotive aeroacoustics: An overview,*
890 *Proceedings of the Institution of Mechanical Engineers, Part D: Jour-*
891 *nal of Automobile Engineering* 231 (2017) 1177–1189. doi:10.1177/
892 0954407017695147.
- 893 [3] H. H. Hubbard, K. P. Shepherd, *Aeroacoustics of large wind turbines,*
894 *The Journal of the Acoustical Society of America* 89 (1991) 2495–2508.
895 doi:10.1121/1.401021.

- 896 [4] G. Minelli, H.-D. Yao, N. Andersson, D. Lindblad, J. Forssén,
897 P. Höstmad, S. Krajnović, Using horizontal sonic crystals to reduce
898 the aeroacoustic signature of a simplified ice3 train model, *Applied*
899 *Acoustics* 172 (2021). doi:10.1016/j.apacoust.2020.107597.
- 900 [5] N. Molin, Airframe noise modeling and prediction, *CEAS Aeronautical*
901 *Journal* 10 (2019) 11–29. doi:10.1007/s13272-019-00375-4.
- 902 [6] W. Dobrzynski, Almost 40 years of airframe noise research: What did
903 we achieve?, *Journal of Aircraft* 47 (2010) 353–367. doi:10.2514/1.
904 44457.
- 905 [7] E. Envia, A. G. Wilson, D. L. Huff, Fan noise: A challenge to caa,
906 *International Journal of Computational Fluid Dynamics* 18 (2004) 471–
907 480. doi:10.1080/10618560410001673489.
- 908 [8] N. Peake, A. B. Parry, Modern challenges facing turbomachinery
909 aeroacoustics, *Annual Review of Fluid Mechanics* 44 (2012) 227–248.
910 doi:10.1146/annurev-fluid-120710-101231.
- 911 [9] D. J. Bodony, S. K. Lele, Current status of jet noise predictions using
912 large-eddy simulation, *AIAA Journal* 46 (2008) 364–380. doi:10.2514/
913 1.24475.
- 914 [10] G. A. Brès, S. K. Lele, Modelling of jet noise: a perspective from large-
915 eddy simulations, *Philosophical Transactions of the Royal Society A:*
916 *Mathematical, Physical and Engineering Sciences* 377 (2019) 20190081.
917 doi:10.1098/rsta.2019.0081.

- 918 [11] A. S. Lyrintzis, M. Coderoni, Overview of the use of large-eddy sim-
919 ulations in jet aeroacoustics, *AIAA Journal* 58 (2020) 1620–1638.
920 doi:10.2514/1.J058498.
- 921 [12] M. J. Lighthill, Report on the Final Panel Discussion on Computational
922 Aeroacoustics, ICASE Report No. 92-53, NASA, Hampton, VA, 1992.
- 923 [13] M. J. Lighthill, On sound generated aerodynamically. i. general theory,
924 *Proceedings of the Royal Society of London. Series A, Mathematical*
925 *and Physical Sciences* 211 (1952) 564–587. doi:10.1098/rspa.1952.
926 0060.
- 927 [14] M. J. Lighthill, On sound generated aerodynamically. ii. turbulence as
928 a source of sound, *Proceedings of the Royal Society of London. Series*
929 *A, Mathematical and Physical Sciences* 222 (1954) 1–32. doi:10.1098/
930 rspa.1954.0049.
- 931 [15] D. Crighton, Basic principles of aerodynamic noise generation,
932 *Progress in Aerospace Sciences* 16 (1975) 31–96. doi:10.1016/
933 0376-0421(75)90010-X.
- 934 [16] F. Farassat, G. Succi, A review of propeller discrete frequency noise
935 prediction technology with emphasis on two current methods for time
936 domain calculations, *Journal of Sound and Vibration* 71 (1980) 399–419.
937 doi:10.1016/0022-460X(80)90422-8.
- 938 [17] K. Brentner, F. Farassat, Helicopter noise prediction: The current status
939 and future direction, *Journal of Sound and Vibration* 170 (1994) 79–96.
940 doi:10.1006/jsvi.1994.1047.

- 941 [18] J. E. Ffowcs Williams, D. L. Hawkings, Sound generation by turbulence
942 and surfaces in arbitrary motion, *Philosophical Transactions of the*
943 *Royal Society of London. Series A, Mathematics and Physical Sciences*
944 264 (1969) 321–342. doi:10.1098/rsta.1969.0031.
- 945 [19] S. K. Lele, J. W. Nichols, A second golden age of aeroacoustics?,
946 *Philosophical Transactions of the Royal Society A: Mathematical, Phys-*
947 *ical and Engineering Sciences* 372 (2014). doi:10.1098/rsta.2013.
948 0321.
- 949 [20] S. Moreau, The third golden age of aeroacoustics, *Physics of Fluids* 34
950 (2022) 031301–1–031301–14. doi:10.1063/5.0084060.
- 951 [21] C. K. Tam, Computational aeroacoustics: An overview of com-
952 putational challenges and applications, *International Journal of*
953 *Computational Fluid Dynamics* 18 (2004) 547–567. doi:10.1080/
954 10618560410001673551.
- 955 [22] T. Colonius, Modeling artificial boundary conditions for compressible
956 flow, *Annual Review of Fluid Mechanics* 36 (2004) 315–345. doi:10.
957 1146/annurev.fluid.36.050802.121930.
- 958 [23] C. K. Tam, J. C. Webb, Dispersion-relation-preserving finite difference
959 schemes for computational acoustics, *Journal of Computational Physics*
960 107 (1993) 262–281. doi:10.1006/jcph.1993.1142.
- 961 [24] S. K. Lele, Compact finite difference schemes with spectral-like reso-
962 lution, *Journal of Computational Physics* 103 (1992) 16–42. doi:10.
963 1016/0021-9991(92)90324-R.

- 964 [25] G. Ashcroft, X. Zhang, Optimized prefactored compact schemes,
965 Journal of Computational Physics 190 (2003) 459–477. doi:10.1016/
966 S0021-9991(03)00293-6.
- 967 [26] T. Poinso, S. Lele, Boundary conditions for direct simulations of com-
968 pressible viscous flows, Journal of Computational Physics 101 (1992)
969 104–129. doi:10.1016/0021-9991(92)90046-2.
- 970 [27] C. K. Tam, Z. Dong, Radiation and outflow boundary conditions for
971 direct computation of acoustic and flow disturbances in a nonuniform
972 mean flow, Journal of Computational Acoustics 4 (1996) 175–201.
973 doi:10.1142/S0218396X96000040.
- 974 [28] T. Z. Dong, On boundary conditions for acoustic computations in non-
975 uniform mean flows, Journal of Computational Acoustics 5 (1997) 297–
976 315. doi:10.1142/S0218396X97000174.
- 977 [29] M. B. Giles, Nonreflecting boundary conditions for euler equation calcu-
978 lations, AIAA Journal 28 (1990) 2050–2058. doi:10.2514/3.10521.
- 979 [30] W. H. Reed, T. Hill, Triangular mesh methods for the neutron trans-
980 port equation, Technical Report LA-UR-73-479, Los Alamos Scientific
981 Laboratory, 1973.
- 982 [31] B. Cockburn, G. E. Karniadakis, C.-W. Shu, The development of
983 discontinuous galerkin methods, in: Discontinuous Galerkin Meth-
984 ods, Springer Berlin Heidelberg, Berlin, Heidelberg, 2000, pp. 3–50.
985 doi:10.1007/978-3-642-59721-3_1.

- 986 [32] H. T. Huynh, A flux reconstruction approach to high-order schemes in-
987 cluding discontinuous galerkin methods, in: 18th AIAA Computational
988 Fluid Dynamics Conference, AIAA Paper 2007-4079, Miami, FL, 2007.
989 doi:10.2514/6.2007-4079.
- 990 [33] D. A. Kopriva, J. H. Kolas, A conservative staggered-grid chebyshev
991 multidomain method for compressible flows, *Journal of Computational*
992 *Physics* 125 (1996) 244–261. doi:10.1006/jcph.1996.0091.
- 993 [34] D. A. Kopriva, A conservative staggered-grid chebyshev multidomain
994 method for compressible flows. ii. a semi-structured method, *Journal*
995 *of Computational Physics* 128 (1996) 475–488. doi:10.1006/jcph.
996 1996.0225.
- 997 [35] D. A. Kopriva, A staggered-grid multidomain spectral method for the
998 compressible navier–stokes equations, *Journal of Computational Physics*
999 143 (1998) 125–158. doi:10.1006/jcph.1998.5956.
- 1000 [36] Y. Liu, M. Vinokur, Z. Wang, Spectral difference method for unstruc-
1001 tured grids i: Basic formulation, *Journal of Computational Physics* 216
1002 (2006) 780–801. doi:10.1016/j.jcp.2006.01.024.
- 1003 [37] G. Karniadakis, S. Sherwin, *Spectral/hp Element Methods for Com-*
1004 *putational Fluid Dynamics*, 2 ed., Oxford University Press, 2005.
1005 doi:10.1093/acprof:oso/9780198528692.001.0001.
- 1006 [38] M. Lorteau, M. de la Llave Plata, V. Couaillier, Turbulent jet simulation
1007 using high-order dg methods for aeroacoustic analysis, *International*

- 1008 Journal of Heat and Fluid Flow 70 (2018) 380 – 390. doi:10.1016/j.
1009 ijheatfluidflow.2018.01.012.
- 1010 [39] M. A. Alhawwary, Z. J. Wang, Implementation of a fwh approach in a
1011 high-order les tool for aeroacoustic noise predictions, in: AIAA Scitech
1012 2020 Forum, AIAA Paper 2020-1724, Orlando, FL, 2020. doi:10.2514/
1013 6.2020-1724.
- 1014 [40] D. Lindblad, S. Sherwin, C. Cantwell, J. Lawrence, A. Proenca, M. Mor-
1015 agues Ginard, Aeroacoustic analysis of a subsonic jet using the discon-
1016 tinuous galerkin method, in: 28th AIAA/CEAS Aeroacoustics Confer-
1017 ence, AIAA Paper 2022-2932, Southampton, UK, 2022. doi:10.2514/
1018 6.2022-2932.
- 1019 [41] R. Modi, M. A. Alhawwary, A. Akbarzadeh, F. Witherden, A. Jame-
1020 son, Aeroacoustics noise prediction for the airfoil-rod benchmark us-
1021 ing high-order large eddy simulation on unstructured grids and the
1022 acoustic analogy approach in frequency-domain, in: AIAA SCITECH
1023 2023 Forum, AIAA Paper 2023-0978, National Harbor, MD, 2023.
1024 doi:10.2514/6.2023-0978.
- 1025 [42] D. Lindblad, S. Sherwin, C. Cantwell, J. Lawrence, A. Proenca, M. Mor-
1026 agues Ginard, Large eddy simulations of isolated and installed jet
1027 noise using the high-order discontinuous galerkin method, in: AIAA
1028 SCITECH 2023 Forum, AIAA Paper 2023-1546, National Harbour, MD,
1029 2023. doi:10.2514/6.2023-1546.
- 1030 [43] C. D. Cantwell, D. Moxey, A. Comerford, A. Bolis, G. Rocco, G. Men-

- 1031 galdo, D. De Grazia, S. Yakovlev, J.-E. Lombard, D. Ekelschot, B. Jordi,
1032 H. Xu, Y. Mohamied, C. Eskilsson, B. Nelson, P. Vos, C. Biotto,
1033 R. Kirby, S. Sherwin, Nektar++: An open-source spectral/hp element
1034 framework, *Computer Physics Communications* 192 (2015) 205 – 219.
1035 doi:10.1016/j.cpc.2015.02.008.
- 1036 [44] D. Moxey, C. D. Cantwell, Y. Bao, A. Cassinelli, G. Castiglioni, S. Chun,
1037 E. Juda, E. Kazemi, K. Lackhove, J. Marcon, G. Mengaldo, D. Serson,
1038 M. Turner, H. Xu, J. Peiró, R. M. Kirby, S. J. Sherwin, Nektar++:
1039 Enhancing the capability and application of high-fidelity spectral/hp
1040 element methods, *Computer Physics Communications* 249 (2020).
1041 doi:10.1016/j.cpc.2019.107110.
- 1042 [45] Antares Development Team, Antares Documentation Release 1.17.0,
1043 2023. URL: <https://cerfacs.fr/antares/>.
- 1044 [46] D. Di Stefano, A. Rona, E. Hall, G. Puigt, Implementing the fflowcs
1045 williams and hawkings acoustic analogy in antares, in: *The 22nd Inter-*
1046 *national Congress on Sound and Vibration (ICSV22)*, Florence, Italy,
1047 2015.
- 1048 [47] D. Di Stefano, A. Rona, E. Hall, C. L. Morfey, G. Puigt, Validating
1049 the fflowcs williams and hawkings acoustic analogy implementation in
1050 antares, in: *22nd AIAA/CEAS Aeroacoustics Conference*, AIAA Paper
1051 2016-3059, Lyon, France, 2016. doi:10.2514/6.2016-3059.
- 1052 [48] F. Farassat, Derivation of Formulations 1 and 1A of Farassat, Technical
1053 Report NASA/TM-2007-214853, NASA, Hampton, VA, 2007.

- 1054 [49] C. Geuzaine, J.-F. Remacle, Gmsh: A 3-d finite element mesh generator
1055 with built-in pre- and post-processing facilities, *International Journal*
1056 *for Numerical Methods in Engineering* 79 (2009) 1309–1331. doi:10.
1057 1002/nme.2579.
- 1058 [50] G. A. Brès, P. Jordan, V. Jaunet, M. Le Rallic, A. V. G. Cavalieri,
1059 A. Towne, S. K. Lele, T. Colonius, O. T. Schmidt, Importance of the
1060 nozzle-exit boundary-layer state in subsonic turbulent jets, *Journal of*
1061 *Fluid Mechanics* 851 (2018) 83–124. doi:10.1017/jfm.2018.476.
- 1062 [51] F. Gand, M. Huet, T. Renaud, F. Sartor, Zdes of jets aeroacoustics:
1063 recent progress with unstructured grids and challenges, in: *AIAA AVI-*
1064 *ATION 2023 FORUM*, San Diego, CA, 2023.
- 1065 [52] D. Moxey, M. D. Green, S. J. Sherwin, J. Peiró, An isoparametric
1066 approach to high-order curvilinear boundary-layer meshing, *Computer*
1067 *Methods in Applied Mechanics and Engineering* 283 (2015) 636–650.
1068 doi:10.1016/j.cma.2014.09.019.
- 1069 [53] The Nektar++ Developer Team, *Nektar++: Spectral/hp Element*
1070 *Framework: User Guide*, 5.3.0 ed., 2023. URL: [https://www.](https://www.nektar.info)
1071 [nektar.info](https://www.nektar.info).
- 1072 [54] The HDF Group, *Hierarchical data format, version 5*, 2023. URL:
1073 <https://www.hdfgroup.org/HDF5/>.
- 1074 [55] Z.-G. Yan, Y. Pan, G. Castiglioni, K. Hillewaert, J. Peiró, D. Moxey,
1075 S. J. Sherwin, *Nektar++: Design and implementation of an implicit,*

- 1076 spectral/hp element, compressible flow solver using a jacobian-free new-
1077 ton krylov approach, *Computers & Mathematics with Applications* 81
1078 (2021) 351–372. doi:10.1016/j.camwa.2020.03.009.
- 1079 [56] R. Hartmann, P. Houston, Symmetric interior penalty dg methods for
1080 the compressible navier-stokes equations i: Method formulation, *Inter-
1081 national Journal of Numerical Analysis and Modeling* 3 (2006) 1–20.
- 1082 [57] G. Mengaldo, D. De Grazia, F. Witherden, A. Farrington, P. Vincent,
1083 S. J. Sherwin, J. Peiro, A guide to the implementation of boundary con-
1084 ditions in compact high-order methods for compressible aerodynamics,
1085 in: 7th AIAA Theoretical Fluid Mechanics Conference, AIAA Paper
1086 2014-2923, Atlanta, GA, 2014. doi:10.2514/6.2014-2923.
- 1087 [58] P. L. Roe, Approximate riemann solvers, parameter vectors, and dif-
1088 ference schemes, *Journal of Computational Physics* 43 (1981) 357–372.
1089 doi:10.1016/0021-9991(81)90128-5.
- 1090 [59] A. Uranga, P.-O. Persson, M. Drela, J. Peraire, Implicit large eddy
1091 simulation of transition to turbulence at low reynolds numbers using
1092 a discontinuous galerkin method, *International Journal for Numerical
1093 Methods in Engineering* 87 (2011) 232–261. doi:10.1002/nme.3036.
- 1094 [60] A. D. Beck, T. Bolemann, D. Flad, H. Frank, G. J. Gassner, F. Hin-
1095 denlang, C.-D. Munz, High-order discontinuous galerkin spectral ele-
1096 ment methods for transitional and turbulent flow simulations, *Inter-
1097 national Journal for Numerical Methods in Fluids* 76 (2014) 522–548.
1098 doi:10.1002/flid.3943.

- 1099 [61] C. Carton de Wiart, K. Hillewaert, L. Briceux, G. Winckelmans,
1100 Implicit les of free and wall-bounded turbulent flows based on the
1101 discontinuous galerkin/symmetric interior penalty method, *International Journal for Numerical Methods in Fluids* 78 (2015) 335–354.
1102 doi:10.1002/flid.4021.
1103
- 1104 [62] M. Bergmann, C. Morsbach, M. Franke, Implicit LES of a Tur-
1105 bulent Channel Flow with High-Order Discontinuous Galerkin and
1106 Finite Volume Discretization, volume 25 of *ERCOFTAC Series*,
1107 Springer International Publishing, 2019, pp. 61–67. doi:10.1007/
1108 978-3-030-04915-7.
- 1109 [63] R. C. Moura, S. J. Sherwin, J. Peiró, Linear dispersion–diffusion anal-
1110 ysis and its application to under-resolved turbulence simulations using
1111 discontinuous galerkin spectral/hp methods, *Journal of Computational*
1112 *Physics* 298 (2015) 695–710. doi:10.1016/j.jcp.2015.06.020.
- 1113 [64] R. C. Moura, G. Mengaldo, J. Peiró, S. J. Sherwin, On the eddy-
1114 resolving capability of high-order discontinuous galerkin approaches to
1115 implicit les / under-resolved dns of euler turbulence, *Journal of Com-*
1116 *putational Physics* 330 (2017) 615–623. doi:10.1016/j.jcp.2016.
1117 10.056.
- 1118 [65] G. Mengaldo, R. C. Moura, B. Giralda, J. Peiró, S. J. Sherwin, Spatial
1119 eigensolution analysis of discontinuous galerkin schemes with practical
1120 insights for under-resolved computations and implicit les, *Computers*
1121 *and Fluids* 169 (2018) 349–364. doi:10.1016/j.compfluid.2017.
1122 09.016.

- 1123 [66] P.-O. Persson, J. Peraire, Sub-cell shock capturing for discontinu-
1124 ous galerkin methods, in: 44th AIAA Aerospace Sciences Meeting
1125 and Exhibit, AIAA 2006-112, Reno, Nevada, 2006. doi:10.2514/6.
1126 2006-112.
- 1127 [67] C. Kennedy, M. Carpenter, Diagonally implicit Runge-Kutta meth-
1128 ods for ordinary differential equations. A review, Technical Report
1129 NASA/TM-2016-219173, NASA, Hampton, VA, 2016.
- 1130 [68] D. A. Knoll, D. E. Keyes, Jacobian-free newton–krylov methods: a sur-
1131 vey of approaches and applications, *Journal of Computational Physics*
1132 193 (2004) 357–397. doi:10.1016/j.jcp.2003.08.010.
- 1133 [69] Y. Saad, M. H. Schultz, Gmres: A generalized minimal residual al-
1134 gorithm for solving nonsymmetric linear systems, *SIAM Journal on*
1135 *Scientific and Statistical Computing* 7 (1986) 856–869. doi:10.1137/
1136 0907058.
- 1137 [70] M. Israeli, S. A. Orszag, Approximation of radiation boundary condi-
1138 tions, *Journal of Computational Physics* 41 (1981) 115–135. doi:10.
1139 1016/0021-9991(81)90082-6.
- 1140 [71] P. Virtanen, R. Gommers, T. E. Oliphant, M. Haberland, T. Reddy,
1141 D. Cournapeau, E. Burovski, P. Peterson, W. Weckesser, J. Bright,
1142 S. J. van der Walt, M. Brett, J. Wilson, K. J. Millman, N. May-
1143 orov, A. R. J. Nelson, E. Jones, R. Kern, E. Larson, C. J. Carey,
1144 Í. Polat, Y. Feng, E. W. Moore, J. VanderPlas, D. Laxalde, J. Perk-
1145 told, R. Cimrman, I. Henriksen, E. A. Quintero, C. R. Harris, A. M.

- 1146 Archibald, A. H. Ribeiro, F. Pedregosa, P. van Mulbregt, SciPy 1.0
1147 Contributors, SciPy 1.0: Fundamental Algorithms for Scientific Com-
1148 puting in Python, *Nature Methods* 17 (2020) 261–272. doi:10.1038/
1149 s41592-019-0686-2.
- 1150 [72] S. Mendez, M. Shoeybi, S. K. Lele, P. Moin, On the use of the fflowcs
1151 williams-hawkings equation to predict far-field jet noise from large-eddy
1152 simulations, *International Journal of Aeroacoustics* 12 (2013) 1–20.
1153 doi:10.1260/1475-472X.12.1-2.1.
- 1154 [73] P. di Francescantonio, A new boundary integral formulation for the pre-
1155 diction of sound radiation, *Journal of Sound and Vibration* 202 (1997)
1156 491–509. doi:10.1006/jsvi.1996.0843.
- 1157 [74] M. L. Shur, P. R. Spalart, M. K. Strelets, Noise prediction for increas-
1158 ingly complex jets. part i: Methods and tests, *International Journal of*
1159 *Aeroacoustics* 4 (2005) 213–245. doi:10.1260/1475472054771376.
- 1160 [75] P. R. Spalart, M. L. Shur, Variants of the fflowcs williams - hawk-
1161 ings equation and their coupling with simulations of hot jets, *In-*
1162 *ternational Journal of Aeroacoustics* 8 (2009) 477–491. doi:10.1260/
1163 147547209788549280.
- 1164 [76] G. Rahier, M. Huet, J. Prieur, Additional terms for the use of fflowcs
1165 williams and hawkings surface integrals in turbulent flows, *Computers*
1166 *and Fluids* 120 (2015) 158–172. doi:10.1016/j.compfluid.2015.
1167 07.014.

- 1168 [77] A. Najafi-Yazdi, G. A. Brès, L. Mongeau, An acoustic analogy formula-
1169 tion for moving sources in uniformly moving media, Proceedings of the
1170 Royal Society A, Mathematical, Physical and Engineering Sciences 467
1171 (2011) 144–165. doi:10.1098/rspa.2010.0172.
- 1172 [78] P. E. Vos, S. J. Sherwin, R. M. Kirby, From h to p effi-
1173 ciently: Implementing finite and spectral/hp element methods to
1174 achieve optimal performance for low- and high-order discretisa-
1175 tions, Journal of Computational Physics 229 (2010) 5161–5181.
1176 URL: [https://www.sciencedirect.com/science/article/
1177 pii/S0021999110001506](https://www.sciencedirect.com/science/article/pii/S0021999110001506). doi:[https://doi.org/10.1016/j.
1178 jcp.2010.03.031](https://doi.org/10.1016/j.jcp.2010.03.031).
- 1179 [79] C. Cantwell, S. Sherwin, R. Kirby, P. Kelly, From h to p ef-
1180 ficiently: Strategy selection for operator evaluation on hexahedral
1181 and tetrahedral elements, Computers and Fluids 43 (2011) 23–28.
1182 URL: [https://www.sciencedirect.com/science/article/
1183 pii/S0045793010002057](https://www.sciencedirect.com/science/article/pii/S0045793010002057). doi:[https://doi.org/10.1016/j.
1184 compfluid.2010.08.012](https://doi.org/10.1016/j.compfluid.2010.08.012), symposium on High Accuracy Flow Sim-
1185 ulations. Special Issue Dedicated to Prof. Michel Deville.
- 1186 [80] D. Moxey, C. Cantwell, R. Kirby, S. Sherwin, Optimising the perfor-
1187 mance of the spectral/hp element method with collective linear alge-
1188 bra operations, Computer Methods in Applied Mechanics and Engi-
1189 neering 310 (2016) 628–645. URL: [https://www.sciencedirect.
1190 com/science/article/pii/S0045782516306739](https://www.sciencedirect.com/science/article/pii/S0045782516306739). doi:<https://doi.org/10.1016/j.cma.2016.07.001>.

- 1192 [81] D. Moxey, R. Amici, M. Kirby, Efficient matrix-free high-order
1193 finite element evaluation for simplicial elements, SIAM Jour-
1194 nal on Scientific Computing 42 (2020) C97–C123. URL: <https://doi.org/10.1137/19M1246523>. doi:10.1137/19M1246523.
1195 [arXiv:https://doi.org/10.1137/19M1246523](https://arxiv.org/abs/1908.08111).
1196
- 1197 [82] A. Proença, J. Lawrence, R. Self, Experimental investigation into the
1198 turbulence flow field of in-flight round jets, AIAA Journal 58 (2020)
1199 1–11. doi:10.2514/1.J059035.
- 1200 [83] C. Bogey, O. Marsden, C. Bailly, Influence of initial turbulence level on
1201 the flow and sound fields of a subsonic jet at a diameter-based reynolds
1202 number of 10^5 , Journal of Fluid Mechanics 701 (2012) 352–385. doi:10.
1203 1017/jfm.2012.162.
- 1204 [84] M. Zhu, C. Pérez Arroyo, A. Fosso Pouangué, M. Sanjosé, S. Moreau,
1205 Isothermal and heated subsonic jet noise using large eddy simulations on
1206 unstructured grids, Computers and Fluids 171 (2018) 166–192. doi:10.
1207 1016/j.compfluid.2018.06.003.
- 1208 [85] F. Gand, M. Huet, On the generation of turbulent inflow for hybrid
1209 rans/les jet flow simulations, Computers and Fluids 216 (2021). doi:10.
1210 1016/j.compfluid.2020.104816.
- 1211 [86] P. Welch, The use of fast fourier transform for the estimation of power
1212 spectra: A method based on time averaging over short, modified peri-
1213 odograms, IEEE Transactions on Audio and Electroacoustics 15 (1967)
1214 70–73. doi:10.1109/TAU.1967.1161901.

- 1215 [87] U. Michel, The role of source interference in jet noise, in: 15th
1216 AIAA/CEAS Aeroacoustics Conference (30th AIAA Aeroacoustics Con-
1217 ference), AIAA Paper 2009-3377, Miami, FL, 2009. doi:10.2514/6.
1218 2009-3377.
- 1219 [88] R. Head, M. Fisher, Jet/surface interaction noise - analysis of farfield
1220 low frequency augmentations of jet noise due to the presence of a solid
1221 shield, in: 3rd Aeroacoustics Conference, AIAA Paper 76-502, Palo
1222 Alto, CA, 1976. doi:10.2514/6.1976-502.
- 1223 [89] S. Ristov, R. Prodan, M. Gusev, K. Skala, Superlinear speedup in hpc
1224 systems: Why and when?, in: 2016 Federated Conference on Computer
1225 Science and Information Systems (FedCSIS), 2016, pp. 889-898.